The Astrophysical Journal, 828:27 (24pp), 2016 September 1 doi:10.3847/0004-637X/828/1/27

WHERE STARS FORM: INSIDE-OUT GROWTH AND COHERENT STAR FORMATION FROM *HST* Hα MAPS OF 3200 GALAXIES ACROSS THE MAIN SEQUENCE AT $0.7 < z < 1.5$

Erica June Nelson[1], Pieter G. van Dokkum[1], Natascha M. Förster Schreiber[2], Marijn Franx[3], Gabriel B. Brammer[4], Ivelina G. Momcheva[1], Stijn Wuyts[2,5], Katherine E. Whitaker[6], Rosalind E. Skelton[7], Mattia Fumagalli[3], Christopher C. Hayward[8,9], Mariska Kriek[10], Ivo Labbé[3], Joel Leja[1], Hans-Walter Rix[11], Linda J. Tacconi[2], Arjen van der Wel[11], Frank C. van den Bosch[1], Pascal A. Oesch[1], Claire Dickey[1], and Johannes Ulf Lange[1]
[1] Astronomy Department, Yale University, New Haven, CT 06511, USA
[2] Max-Planck-Institut für extraterrestrische Physik, Giessenbachstrasse, D-85748 Garching, Germany
[3] Leiden Observatory, Leiden University, Leiden, The Netherlands
[4] Space Telescope Science Institute, 3700 San Martin Drive, Baltimore, MD 21218, USA
[5] Department of Physics, University of Bath, Claverton Down, Bath, BA2 7AY, UK
[6] Astrophysics Science Division, Goddard Space Flight Center, Greenbelt, MD 20771, USA
[7] South African Astronomical Observatory, P.O. Box 9, Observatory, 7935, South Africa
[8] TAPIR, California Institute of Technology, Pasadena, CA 91125, USA
[9] Harvard-Smithsonian CfA, Cambridge, MA 02138, USA
[10] Department of Astronomy, University of California, Berkeley, CA 94720, USA
[11] Max Planck Institute for Astronomy (MPIA), Königstuhl 17, D-69117, Heidelberg, Germany
Received 2015 July 10; revised 2016 May 30; accepted 2016 June 9; published 2016 August 25

ABSTRACT

We present Hα maps at 1 kpc spatial resolution for star-forming galaxies at $z \sim 1$, made possible by the Wide Field Camera 3 grism on *Hubble Space Telescope* (*HST*). Employing this capability over all five 3D-*HST*/CANDELS fields provides a sample of 3200 galaxies enabling a division into subsamples based on stellar mass and star formation rate (SFR). By creating deep stacked Hα images, we reach surface brightness limits of 1×10^{-18} erg s^{-1} cm^{-2} arcsec^{-2}, allowing us to map the distribution of ionized gas to ∼10 kpc for typical L^* galaxies at this epoch. We find that the spatial extent of the Hα distribution increases with stellar mass as $r_{\rm H\alpha} = 1.5(M_*/10^{10}\,M_\odot)^{0.23}$ kpc. The Hα emission is more extended than the stellar continuum emission, consistent with inside-out assembly of galactic disks. This effect grows stronger with mass as $r_{\rm H\alpha}/r_* = 1.1\,(M_*/10^{10}\,M_\odot)^{0.054}$. We map the Hα distribution as a function of SFR(IR+UV) and find evidence for "coherent star formation" across the SFR–M_* plane: above the main sequence (MS), Hα is enhanced at all radii; below the MS, Hα is depressed at all radii. This suggests that at all masses the physical processes driving the enhancement or suppression of star formation act throughout the disks of galaxies. At high masses ($10^{10.5} < M_*/M_\odot < 10^{11}$), above the MS, Hα is particularly enhanced in the center, potentially building bulges and/or supermassive black holes. Below the MS, a strong central dip in the EW(Hα), as well as the inferred specific SFR, appears. Importantly, though, across the entirety of the SFR–M_* plane, the absolute SFR as traced by Hα is always centrally peaked, even in galaxies below the MS.

Key words: galaxies: evolution – galaxies: formation – galaxies: high-redshift – galaxies: star formation – galaxies: structure

1. INTRODUCTION

The structural formation history of galaxies is written by the spatial distribution of their star formation through cosmic time. Recently, the combination of empirical modeling and observations of the scaling relation between stellar mass and star formation rate (SFR) has enabled us to constrain the buildup of stellar mass in galaxies over a large fraction of cosmic time (Yang et al. 2012; Behroozi et al. 2013; Leja et al. 2013; Moster et al. 2013; Lu et al. 2014; Whitaker et al. 2014). The dawn of Wide Field Camera 3 (WFC3) on the *Hubble Space Telescope* (*HST*) has enabled us to map the structural growth of this stellar mass content of galaxies at high fidelity over a large fraction of the history of the universe (e.g., Wuyts et al. 2011b, 2012; van der Wel et al. 2012, 2014a, 2014b; Bruce et al. 2014; Boada et al. 2015; Peth et al. 2016). It has become clear that the physical sizes of galaxies increase with cosmic time as the universe expands (Giavalisco et al. 1996; Ferguson et al. 2004; Trujillo et al. 2006; Toft et al. 2007; Buitrago et al. 2008; Franx et al. 2008; Kriek et al. 2009; Oesch et al. 2010; Williams et al. 2010; Mosleh et al. 2012; van der Wel et al. 2014b). For star-forming galaxies, with increasing stellar mass, the disk scale length increases, as does the prominence of the bulge (e.g., Shen et al. 2003; Buitrago et al. 2013; Lang et al. 2014). The picture that has emerged from these studies is that most galaxies form their stars in disks growing inside out (van Dokkum et al. 2010; Wuyts et al. 2011b, 2013; La Barbera et al. 2012; Abramson et al. 2014; van der Wel et al. 2014a).

In the canonical paradigm, inside-out growth is a consequence of the dark matter halo properties of the galaxies. Galaxies are thought to accrete their gas from the cosmic web at a rate throttled by the mass of their dark matter halo (e.g., White & Rees 1978; Dekel et al. 2013). The gas cools onto the disk of the galaxy and forms stars with a radial distribution set by the angular momentum distribution of the halo (Fall & Efstathiou 1980; Dalcanton et al. 1997; van den Bosch 2001). As the scale factor of the universe increases, so does the spatial extent of the gas (Mo et al. 1998); galaxies were smaller in the past and grow larger with time, building up from the inside out. However, the actual formation of galaxies in a cosmological context is more complex (e.g., van den Bosch 2001; Hummels & Bryan 2012). Recently, significant progress has been made by the creation of realistic disk galaxies in hydrodynamical

simulations (Governato et al. 2010; Agertz et al. 2011; Brooks et al. 2011; Guedes et al. 2011; Aumer et al. 2013; Marinacci et al. 2013; Stinson et al. 2013) and combining theory and observations in a self-consistent framework (Dekel & Birnboim 2006; Genzel et al. 2008, 2011; Dekel et al. 2009a; Förster Schreiber et al. 2009, 2011a; Keres et al. 2009; Wuyts et al. 2011a, 2011b). How gas is accreted onto galaxies (e.g., Brooks et al. 2009; Sales et al. 2012) and feedback (e.g., Keres et al. 2005; Sales et al. 2010; Übler et al. 2014; Genel et al. 2015; Minchev et al. 2015; Nelson et al. 2015) have been shown to be essential ingredients. However, precisely what physical processes drive the sizes, morphologies, and evolution of disk galaxies is still a matter of much debate (see, e.g., Dutton & van den Bosch 2012; Ferreras et al. 2012; Scannapieco et al. 2012).

Furthermore, the evidence for this picture is indirect: we do not actually observe star formation building up different parts of these galaxies. Instead, we infer it based on empirically linking galaxies across cosmic time and tracking radial changes in stellar surface densities and structural parameters (van Dokkum et al. 2010, 2013; Wuyts et al. 2011b; Patel et al. 2013; van der Wel et al. 2014b; Brennan et al. 2015; Papovich et al. 2015). However, this method has uncertainties due to scatter in stellar mass growth rates and merging (e.g., Behroozi et al. 2013; Leja et al. 2013). Furthermore, migration and secular evolution may have changed the orbits of stars after their formation such that they no longer live in their birthplaces (e.g., Roškar et al. 2008).

The missing piece is a direct measurement of the spatial distribution of star formation within galaxies. This is crucial to understanding the integrated relations of galaxy growth between SFR and M_*. The spatial distribution of star formation yields insights into what processes drive the star formation activity, evolution of stellar mass, and the relation between them. It helps to disentangle the role of gas accretion, mergers, and secular evolution on the assembly history of galaxies. Furthermore, this provides a test of inside-out growth, which appears to be a crucial feature of galaxy assembly history.

What is required is high spatial resolution maps of star formation and stellar continuum emission for large samples of galaxies while they were actively forming their disks. The Hα flux scales with the quantity of ionizing photons produced by hot young stars, serving as an excellent probe of the sites of ongoing star formation activity (Kennicutt 1998). A number of large surveys have used Hα to probe the growth of evolving galaxies, including recently HiZELS (Geach et al. 2008; Sobral et al. 2009), WISP (Atek et al. 2010), MASSIV (Contini et al. 2012), SINS/zC-SINF (Förster Schreiber et al. 2006, 2009), KROSS (Stott et al. 2014), and KMOS^{3D} (Wisnioski et al. 2015). Broadband rest-frame optical imaging provides information on the stellar component. The spatial distribution of this stellar light contains a record of past dynamical processes and the history of star formation. The comparison of the spatial distribution of ionized gas and stellar continuum emission thus provides an essential lever arm for constraining the structural assembly of galaxies. This potent combination shed light on the turbulent early phase of massive galaxy growth at $z \sim 2$ (Förster Schreiber et al. 2011a; Epinat et al. 2012; Buitrago et al. 2014; Genzel et al. 2014b; Tacchella et al. 2015a, 2015b) and the spatially resolved star-forming sequence (Wuyts et al. 2013). To apply this same methodology to a global structural analysis requires high spatial resolution spectroscopic measurements for a large sample of galaxies. An ideal data set would also contain broadband optical imaging with the same high spatial resolution to allow for robust comparison of the spatial distribution of ionized gas and stellar continuum emission.

This has now become possible with the WFC3 grism capability on *HST*. The combination of WFC3's high spatial resolution and the grism's low spectral resolution provides spatially resolved spectroscopy. Because this spectrograph is slitless, it provides a spectrum for every object in its field of view. This means that for every object in its field of view and wavelength coverage, the grism can be used to create a high spatial resolution emission-line map. The 3D-*HST* legacy program utilizes this powerful feature for a 248-orbit near-IR (NIR) imaging and grism spectroscopic survey over the five CANDELS fields (van Dokkum et al. 2011; Brammer et al. 2012b; Momcheva et al. 2016). In this paper, we use data from the 3D-*HST* survey to map the spatial distribution of Hα emission (a tracer of star formation) and $H_{\rm F140W}$ stellar continuum emission (rest-frame 7000 Å, a proxy for the stellar mass) for a sample of 3200 galaxies at $0.7 < z < 1.5$. The Hα and stellar continua are resolved on scales of $0\farcs13$. This represents the largest survey to date of the spatially resolved properties of the Hα distribution in galaxies at any epoch. This spatial resolution, corresponding to 1.1 kpc, is necessary for structural analysis and only possible from the ground with adaptive optics (AO) assisted observations on 10 m class telescopes. This data set hence provides a link between the high spatial resolution imaging data sets of large samples of galaxies with *HST* and high spatial resolution emission-line maps of necessarily small samples with AO on large ground-based telescopes. This study complements the large MOSDEF (Kriek et al. 2015) and KMOS^{3D} (Wisnioski et al. 2015) spectroscopic surveys by providing higher spatial resolution emission-line measurements.

We present the average surface brightness profiles of Hα and stellar continuum emission in galaxies during the epoch $0.7 < z < 1.5$. We analyze Hα maps for 3200 galaxies from the 3D-*HST* survey to trace the spatial distribution of star formation. Our sample cuts a large swath through the SFR–M_* plane covering two orders of magnitude in stellar mass $10^9 < M_* < 10^{11}$ and SFR $1 < \mathrm{SFR} < 400\,M_\odot\,\mathrm{yr}^{-1}$ and encompassing the star-forming "main sequence" (MS). Wuyts et al. (2012) showed that the bright, visually striking clumps of star formation that appear to be common in high-redshift galaxies are short-lived and contribute little to the integrated SFR of a galaxy. Here we average over these short-lived clumps by stacking Hα maps. Stacking thousands of *HST* orbits provides deep average Hα images that allow us to trace the Hα distribution down to a surface brightness limit of $1 \times 10^{-18}\,\mathrm{erg\,s^{-1}\,cm^{-2}\,arcsec^{-2}}$ in our deepest stacks, an order of magnitude fainter than previous studies in the high-redshift universe. This enables us to measure the star formation surface density down to a limit of $4 \times 10^{-4}\,M_\odot\,\mathrm{yr^{-1}\,kpc^{-2}}$. With these deep stacked images, the primary goals of this study are to derive the average surface brightness profile and effective radius of Hα as a function of mass and SFR to provide insight into where star formation occurs in galaxies at this epoch.

2. DATA

2.1. The 3D-HST Survey

We investigate the spatial distribution of star formation in galaxies during the epoch spanning $0.7 < z < 1.5$ across the SFR–M_* plane using data from the 3D-*HST* survey. 3D-*HST* is a 248-orbit extragalactic treasury program with *HST* furnishing NIR imaging and grism spectroscopy across a wide field (van Dokkum et al. 2011; Brammer et al. 2012b; Momcheva et al. 2016). *HST*'s G141 grism on WFC3 provides spatially resolved spectra of all objects in the field of view. The G141 grism has a wavelength range of $1.15\ \mu\mathrm{m} < \lambda < 1.65\ \mu\mathrm{m}$, covering the H$\alpha$ emission line for $0.7 < z < 1.5$. Combined with the accompanying H_{F140W} imaging, 3D-*HST* enables us to derive the spatial distribution of Hα and rest-frame *R*-band emission with matching 1 kpc resolution for an objectively selected sample of galaxies.

The program covers the well-studied CANDELS fields (Grogin et al. 2011; Koekemoer et al. 2011) AEGIS, COSMOS, GOODS-S, UDS, and also includes GOODS-N (GO-11600, PI: B. Weiner). The optical and NIR imaging from CANDELS, in conjunction with the bountiful public photometric data from 0.3 to 24 μm, provides stringent constraints on the spectral energy distributions (SEDs) of galaxies in these fields (Skelton et al. 2014).

2.2. Determining z, M_*, SFR

This study depends on robustly determining galaxy integrated properties, specifically M_* and SFR. Both of these quantities in turn depend on a robust determination of redshift and constraints on the SEDs of galaxies across the electromagnetic spectrum. To do this, the photometric data were shepherded and aperture photometry was performed to construct PSF-matched, deblended, $J_{F125W}/H_{F140W}/H_{F160W}$ selected photometric catalogs (see Skelton et al. 2014). These photometric catalogs form the scaffolding of this project upon which all the remaining data products rest. For this study, we rely on the rest-frame colors, stellar masses, and SFRs. All of these quantities were derived based on constraints from across the electromagnetic spectrum.

Our redshift fitting method also utilizes the photometry. This is probably not strictly necessary for the sample of Hα line emitting galaxies used for this study, although it helps to confirm the redshift of galaxies with only one emission line detected. It is crucial, however, for galaxies without significant emission or absorption features falling in the grism spectrum. To measure redshifts, the photometry and the two-dimensional G141 spectrum were fit simultaneously with a modified version of the EAzY code (Brammer et al. 2008). After finding the best redshift, emission-line strengths were measured for all lines that fall in the grism wavelength range (see Momcheva et al. 2016).

Galaxy stellar masses were derived using stellar population synthesis modeling of the photometry with the FAST code (Kriek et al. 2009). We used the Bruzual & Charlot (2003) templates with solar metallicity and a Chabrier (2003) initial mass function. We assumed exponentially declining star formation histories and the Calzetti et al. (2000) dust attenuation law (see Skelton et al. 2014). Errors in the stellar mass due to contamination of the broadband flux by emission lines are not expected to be significant for this study (see the Appendix in Whitaker et al. 2014). Additionally, the assumption of solar metallicity for all galaxies is simplistic. Galaxies follow a mass–metallicity relation, so low-mass galaxies have significantly subsolar metallicity. This assumption is ameliorated somewhat by the correlation between mass-to-light ratio (M/L) and color independent of metallicity (Bell & de Jong 2001). However, stellar mass estimates could still be affected by up to 0.3 dex (Mitchell et al. 2013). Because we cannot constrain the metallicity, and to make comparison to other studies more straightforward, we adopt a fixed solar metallicity for all galaxies in the fitting process.

Galaxy SFRs in this work were computed by summing unobscured (UV) plus dust absorbed and re-emitted emission (IR) from young stars:

$$\begin{aligned}\mathrm{SFR} &= \mathrm{SFR}_{\mathrm{UV+IR}}(M_\odot \mathrm{yr}^{-1}) \\ &= 1.09 \times 10^{-10}(L_{\mathrm{IR}} + 2.2L_{\mathrm{UV}})/L_\odot \end{aligned} \quad (1)$$

(Bell et al. 2005). L_{UV} is the total UV luminosity from 1216 to 3000 Å. It is derived by scaling the rest-frame 2800 Å luminosity determined from the best-fit SED with EAzY (Brammer et al. 2008). L_{IR} is the total IR luminosity from 8 to 1000 μm. It is derived by scaling the MIPS 24 μm flux density using a luminosity-independent template that is the log average of the Dale & Helou (2002) templates with $1 < \alpha < 2.5$ (Franx et al. 2008; Wuyts et al. 2008; Muzzin et al. 2010). See Whitaker et al. (2014) for more details. We note that both the UV and IR luminosities can be contaminated by older stellar populations and thus potentially overestimate the true SFR; however, the galaxies studied in this work generally have sSFR $\gtrsim 10^{-10}$ yr^{-1}, a regime for which the $\mathrm{SFR}_{\mathrm{UV+IR}}$ traces the true SFR well (Hayward et al. 2014; Utomo et al. 2014).

Table 1
Galaxy Selection Criteria

$0.75 < z < 1.5$
$9.0 < \log(M_*) < 11$
$U - V > 0.8(V - J) + 0.6$ and $U - V > 1.3$ and $V - J < 1.5$
$H_{F140W} \leqslant 24$
$F(\mathrm{H}\alpha) > 0 \times 10^{-17}$ erg s^{-1} cm^{-2}
Flag(galfit) > 2[a]
$L_x > 10^{42.5}$ erg s^{-1}
$\sigma < 2000$ km s^{-1}
Not badly contaminated

Note.
[a] Corresponds to objects with bad or nonexistent galfit fit (van der Wel et al. 2012).

2.3. Sample Selection

Our galaxy selection criteria are outlined in Table 1. We consider all galaxies (1) in the redshift range $0.7 < z < 1.5$ for which the Hα emission line falls in the G141 grism wavelength coverage; (2) that have stellar masses $9.0 < \log(M_*) < 11.0$, a mass range over which our *H*-band selected catalogs are complete; and (3) that are characterized as star-forming according to the *UVJ*-color criterion based on SED shape (Labbe et al. 2005; Wuyts et al. 2007; Whitaker et al. 2011). The *UVJ* selection separates quiescent galaxies from star-forming galaxies using the strength of the Balmer/4000 Å break that is sampled by the rest-frame $U - V$ and $V - J$ colors. These three criteria result in a parent sample of 8068 star-forming galaxies. The grism spectra are fit down to $H_{F140W} = 24$, trimming the sample to 6386 and meaning that we are less complete at low

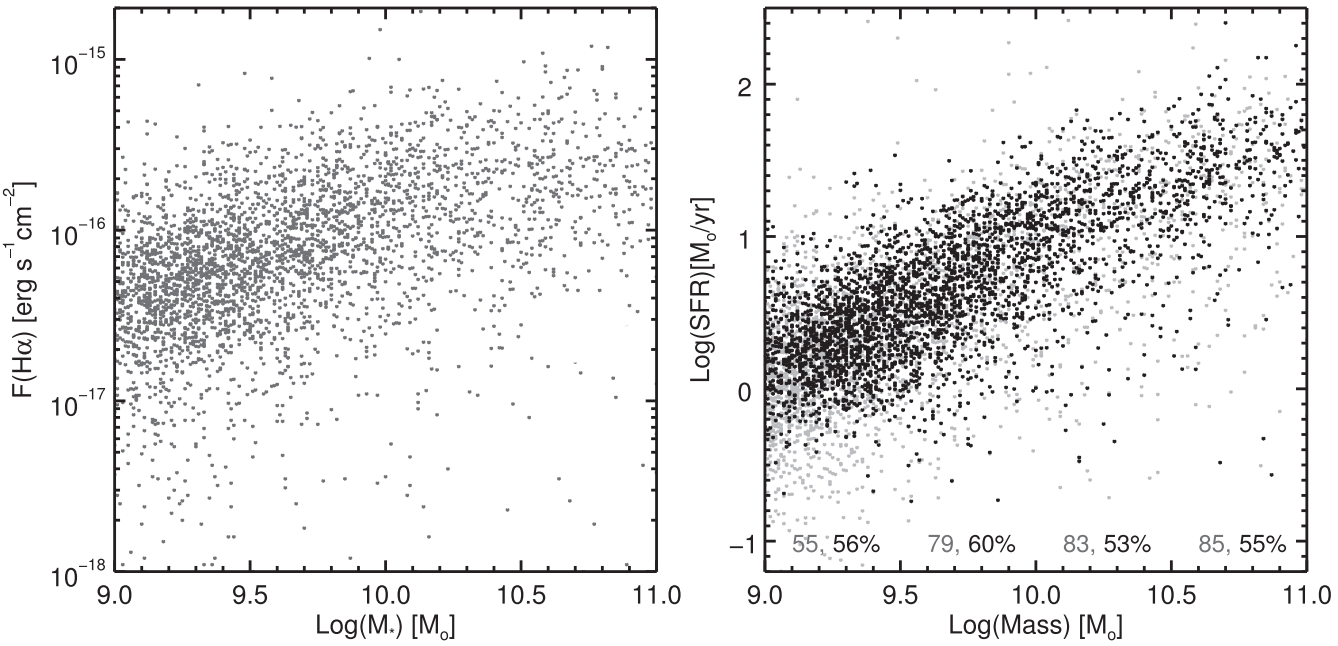

Figure 1. Sample selection. The left panel shows the locus of galaxies in the $F(\mathrm{H}\alpha)$-M_* plane. The right panel shows the distribution of our sample in the SFR–M_* plane. The SFRs come from the UV+IR. The parent sample is shown in gray; selected galaxies are shown in black. The fraction of the total parent sample above the extraction magnitude limit in each 0.5 dex mass range is listed at the bottom in gray. As expected, we are less complete at low masses and SFRs. About one-third of galaxies are removed due to contamination of their spectra by other sources in the field. Of the galaxies above the extraction limit, the fractions remaining as part of the final selection are listed in black. Our sample contains 3200 galaxies from $0.7 < z < 1.5$ spanning 2 decades in M_* and SFR.

masses and SFRs. We require only that the $F(\mathrm{H}\alpha) > 0.0$, but we checked that imposing a more stringent limit on the Hα flux does not change our results.

We exclude 322 galaxies that were flagged as having bad GALFIT (Peng et al. 2002) fits in the van der Wel et al. (2014b) catalogs, often indicative of oddities in the photometry. We identify galaxies that are likely to host active galactic nuclei (AGNs) as sources with X-ray luminosity $L_x > 10^{42.5}$ erg s^{-1} or Hα emission line widths of $\sigma > 2000$ km s^{-1} (see next section). The X-ray luminosities were derived by matching the 3D-*HST* catalog to the publicly available catalog from the NASA High Energy Astrophysics Archive Research Center, noting, however, that the X-ray coverage in these fields is not uniform. We remove these 107 galaxies from the sample as emission from AGNs would complicate the interpretation of the measured Hα distributions.

Finally, of this sample, we discard 33% of galaxies due to contamination of their spectra by the spectra of other nearby objects (see next section for more detail). The contaminating spectra are primarily bright stars and galaxies unrelated to the object, but it is possible that this criterion might lead to a slight bias against denser environments. The fraction of galaxies removed from the sample due to contamination does not vary with stellar mass or SFR. The final sample contains 3200 galaxies and is shown in Figure 1.

3. ANALYSIS

3.1. Morphological Information in the Spectrum

The Hα maps at the heart of this analysis are created from the two-dimensional 3D-*HST* grism spectra. The creation of Hα emission line maps is possible as a consequence of a unique interaction of features: WFC3 has high spatial resolution (0.″14), and the G141 grism has low ($R \sim 130$) point-source spectral resolution. A G141 grism spectrum is a series of high-resolution images of a galaxy taken at 46 Å increments and placed next to each other on the WFC3 detector. An emission line in such a setup effectively emerges as an image of the galaxy in that line superimposed on the continuum. A resolution element for a galaxy at $z \sim 1$ corresponds to a velocity dispersion of $\sigma \sim 1000$ km s^{-1}, so a spectrum will only yield velocity information about a galaxy if the velocity difference across that galaxy is more than 1000 km s^{-1}. Few galaxies have such large line widths. Thus, in general, structure in an emission line is due to *morphology*, not kinematics. While in a typical ground-based spectroscopy the shape of the emission line yields spectral information, in our spectra it yields spatial information. The upshot of this property is that by subtracting the continuum from a spectrum, we obtain an emission-line map of that galaxy. A sample G141 spectrum is shown in Figure 2, and sample Hα maps are shown in Figure 3.

We note that although it is generally true that the spectral axes of these Hα maps do not contain kinematic information, there is one interesting exception: broad-line AGNs. With line widths of >1000 km s^{-1}, the spectra of these objects do contain kinematic information. These sources are very easy to pick out: they appear as point sources in the spatial direction and extended in the spectral direction.

Furthermore, because the WFC3 camera has no slits, we get a 2D spectrum of every object in the camera's field of view. For all galaxies with $0.7 < z < 1.5$ that have an Hα emission line in G141's wavelength coverage, we obtain an Hα map to the surface brightness limits. Based on our selection criteria, using this methodology, we have a sample of 3200 galaxies at $0.7 < z < 1.5$ with spatially resolved Hα information.

3.2. Making Hα maps

The reduction of the 3D-*HST* spectroscopy with the G141 grism and imaging with the H_{F140W} filter was done using a

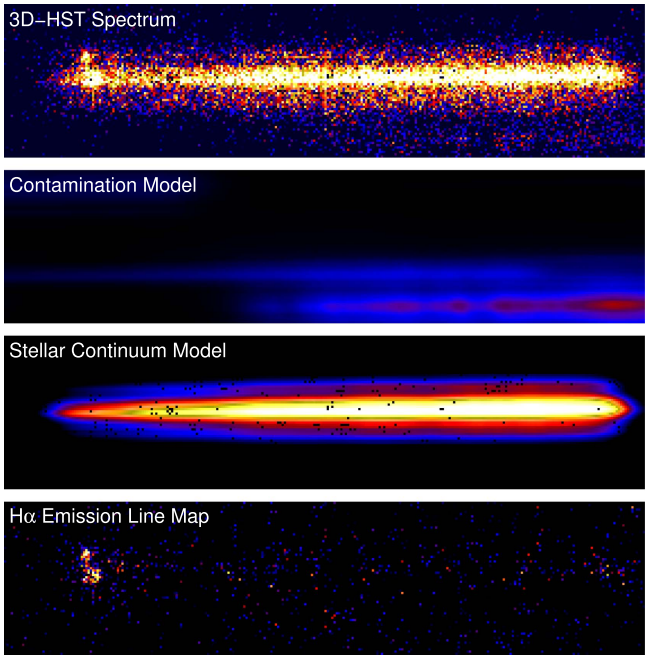

Figure 2. Illustration of the creation of Hα emission line maps from *HST* WFC3 grism data. The top panel shows the 2D, interlaced grism spectrum. The second panel shows a model for the "contamination": the spectra of all objects in the field except the object of interest. The third panel is a 2D model for the continuum emission of the galaxy. The bottom panel is the original spectrum with the contaminating emission from other obejcts, as well as the stellar continuum, subtracted. The result is a 2D map of the line emission at the spatial resolution of *HST* (see Section 3.2 for details).

custom pipeline. *HST* data are typically reduced by drizzling, but the observing strategy of 3D-*HST* allows images to be interlaced instead. With this dither pattern, four images are taken with pointing offsets that are multiples of half pixels. The pixels from these four uncorrected frames are then placed on an output grid with 0.″06 pixels (van Dokkum et al. 2000). Interlacing improves the preservation of spatial information, effectively improving the spatial resolution of the images. Crucially, interlacing also eliminates the correlated noise caused by drizzling. This correlated noise is problematic for analysis of spectroscopic data because it can masquerade as spectral features.

Although the background levels in NIR images taken from space are lower than in those taken from Earth, they are still significant. The modeling of the background in the grism data is complicated because it is composed of many faint higher-order spectra. It is done using a linear combination of three physical eigen-backgrounds: zodiacal light, metastable He emission (Brammer et al. 2014), and scattered light from the Earth limb (G. B. Brammer et al. 2016, in preparation). Residual background structure in the wavelength direction of the frames is fit and subtracted along the image columns. (For more information see Brammer et al. 2012b, 2014; Momcheva et al. 2016). The 2D spectra are extracted from the interlaced G141 frames around a spectral trace based on a geometrical mapping from the location of their F140W direct image positions. A sample 2D spectrum and a pictorial depiction of the remainder of this subsection is shown in Figure 2.

The advantage of slitless spectroscopy is also its greatest challenge: flux from neighboring objects with overlapping traces can contaminate the spectrum of an object with flux that does not belong to it. We forward-model contamination with a flat spectrum based on the direct image positions and morphologies of contaminating objects. A second iteration is done to improve the models of bright ($H < 22$) sources using their extracted spectra. An example of this contamination model is shown in the second panel of Figure 2 (see Brammer et al. 2012a, 2012b, 2013; Momcheva et al. 2016). To remove contamination from the spectra, we subtract these models for all galaxies in the vicinity of the object of interest. Furthermore, for the present analysis, all regions predicted to have contamination that is greater than one-third of the average G141 background value were masked. This aggressive masking strategy was used to reduce the uncertainty in the interpretation of the Hα maps at large radii where uncertainties in the contamination model could introduce systematics.

The continuum of a galaxy is modeled by convolving the best-fit SED without emission lines with its combined $J_{F125W}/H_{F140W}/H_{F160W}$ image. The continuum model for our example galaxy is shown in the third panel of Figure 2. This continuum model is subtracted from the 2D grism spectrum, removing the continuum emission and simultaneously correcting the emission-line maps for stellar absorption. What remains for galaxies with $0.7 < z < 1.5$ is a map of their Hα emission. Five sample Hα maps and their corresponding $H_{\rm F140W}$ images are shown in Figure 3. Crucially, the Hα and stellar continuum images were taken with the same camera under the same conditions. This means that differences in their spatial distributions are intrinsic, not due to differences in the point-spread function (PSF). The spatial resolution is ∼1 kpc for both the $H_{\rm F140W}$ stellar continuum and Hα emission line maps.

The final postage stamps we use in this analysis are 80 × 80 pixels. An *HST* pixel is 0.″06, so this corresponds to 4.8 × 4.″8 or 38 × 38 kpc at $z \sim 1$. Many of these postage stamps have a small residual positive background (smaller than the noise). To correct for this background, we compute the median of all unmasked pixels in the 2 kpc edges of each stamp and subtract it. This means that we can reliably trace the surface brightness out to a maximum of 17 kpc. Beyond this point, the surface brightness is definitionally zero.

3.3. Stacking

To measure the average spatial distribution of Hα during this epoch from $z = 1.5$ to 0.7, we create mean Hα images by stacking the Hα maps of individual galaxies with similar M_* and/or SFR (See Sections 4 and 5). Many studies first use Hα images of individual galaxies to measure the spatial distribution of star formation and then describe average trends in this distribution as a function of M_* or SFR (e.g., Förster Schreiber et al. 2006, 2009; Epinat et al. 2009, 2012; Genzel et al. 2011, 2014b; Contini et al. 2012; Nelson et al. 2012; Wuyts et al. 2013). Instead, we first create average Hα images by stacking galaxies as a function of M_* and SFR and then measure the spatial distribution of star formation to describe trends. This stacking strategy leverages the strengths of our data: Hα maps taken under uniform observing conditions for a large and objectively defined sample of galaxies. From a practical standpoint, the methodology has the advantage that we do not need data with very high signal-to-noise ratio (S/N). As a consequence, we can explore relatively uncharted regions of parameter space. In particular, we can measure the radial distribution of star formation in galaxies across a vast expanse of the SFR–M_* plane down to low masses and SFRs.

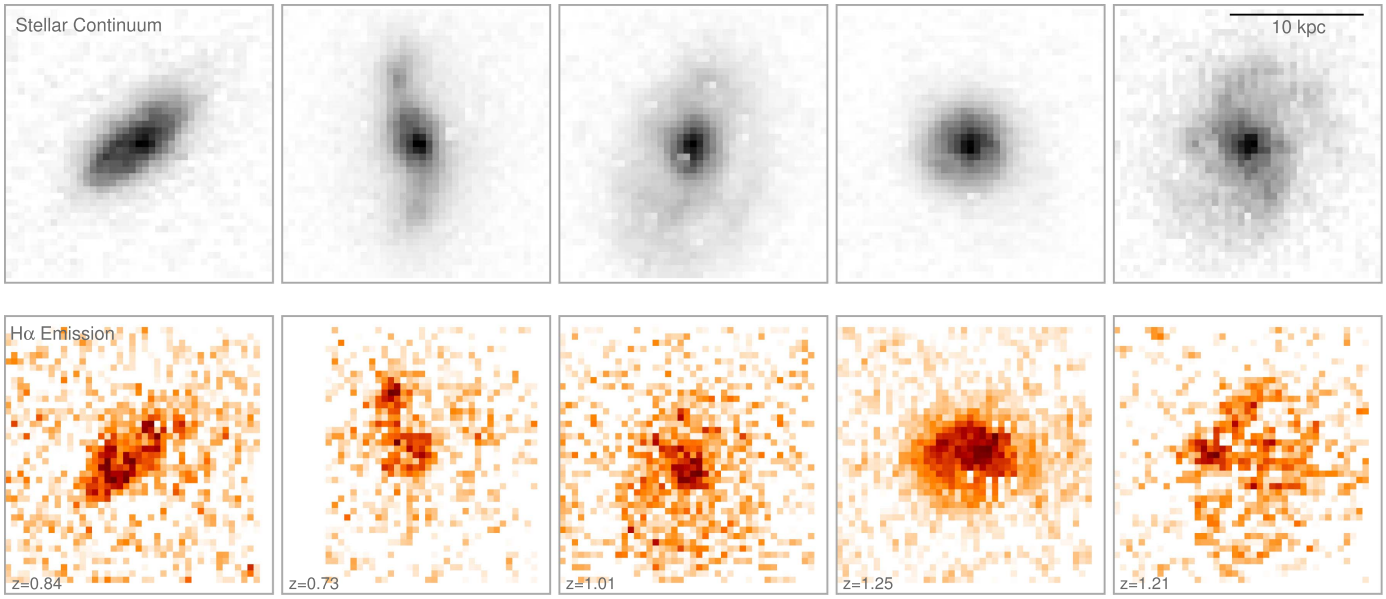

Figure 3. High-resolution Hα maps for $z \sim 1$ galaxies from *HST* and their corresponding rest-frame optical images. The Hα generally follows the optical light, but not always (see also Wuyts et al. 2013).

Additionally, we can probe the distribution of ionized gas in the outer regions of galaxies where star formation surface densities are thought to be very low.

We created the stacked images by summing normalized, masked images of galaxies in $H_{\rm F140W}$ and Hα. To best control for the various systematics described in the remainder of this section, for our primary analysis, we do not distort the galaxy images by deprojecting, rotating, or scaling them. We show major-axis aligned stacks in Section 6 and deprojected, radially normalized profiles in the Appendix. Our results remain qualitatively consistent regardless of this methodological decision. For all analyses, the images were weighted by their $H_{\rm F140W}$ flux, so the stack is not dominated by a single bright object. The $H_{\rm F140W}$ filter covers the full wavelength range of the G141 grism encompassing the Hα emission line. Normalizing by the $H_{\rm F140W}$ emission hence accounts for very bright Hα line emission without inverse S/N weighting as normalizing by the Hα emission would.

As a consequence of the grism's low spectral resolution, we have to account for the blending of emission lines. With an FWHM spectral resolution of $\sim$100 Å, Hα λ6563 and [N II] $\lambda\lambda$6548 + 6583 are blended. To account for the contamination of Hα by [N II], we scale the measured flux down by a factor of $\mathrm{H}\alpha_{\rm corr} = \mathrm{H}\alpha_{\rm meas}/(1+[\mathrm{N\ II}]/\mathrm{H}\alpha)$ and adopt $\mathrm{H}\alpha_{\rm corr}$ as the Hα flux. [N II]/Hα varies between galaxies (e.g., Savaglio et al. 2005; Erb et al. 2006a; Maiolino et al. 2008; Leja et al. 2013; Zahid et al. 2013; Wuyts et al. 2014; Sanders et al. 2015; Shapley et al. 2015; Sobral et al. 2015), as well as radially within galaxies (e.g., Yuan et al. 2011; Queyrel et al. 2012; Swinbank et al. 2012; Jones et al. 2013, 2015; Förster Schreiber et al. 2014; Genzel et al. 2014a; Stott et al. 2014). Stott et al. (2014) and E. Wuyts et al. (2016) find a range of metallicity gradients -0.063 dex kpc$^{-1} < \Delta Z/\Delta r < 0.073$ dex kpc^{-1}. On average, [N II]/Hα gradients are flat. So as not to introduce systematic uncertainties into the data, we do not adopt a radial gradient, but instead a single normalization factor for each stack. We compute this normalization with the [N II]/Hα–EW(Hα + [N II]) relation of Sobral et al. (2015) using the median EW(Hα + [N II]) of each stack. With this relation we derive ratios ranging from [N II]/H$\alpha \sim 0.05$ in low-mass galaxies above the MS to [N II]/H$\alpha \sim 0.3$ in high-mass galaxies below it. So, in general the corrections to the Hα surface brightness are small.

Additionally, Hα λ6563 and [S II] $\lambda\lambda$6716, 6731 are resolved but are separated by only about three resolution elements. In this study, we are concerned primarily with the radial distribution of Hα emission. In order to prevent [S II] from adding flux at large radii, we mask the region of the 2D spectrum redward of Hα where [S II] emission could contaminate the Hα maps.

Galaxies are centered according to the light-weighted center of their $H_{\rm F140W}$ flux distribution. Given that the $H_{\rm F140W}$ can be used as a proxy for stellar mass, we chose to center the galaxies according to their $H_{\rm F140W}$ center as our best approximation of centering them according to stellar mass. While the $H_{\rm F140W}$ centroid will not always be the exact center of mass, it is a better estimate than our other option, the Hα centroid. We measure the centroid of the $H_{\rm F140W}$ images as the flux-weighted mean pixel in the x- and y- directions independently with an algorithm similar to the IRAF task imcntr. We shift the $H_{\rm F140W}$ image with subpixel shifts using damped sinc interpolation. The G141 image is shifted with the same shifts. To center the Hα map requires only a geometric mapping in the spatial direction of the 2D grism spectrum. In the spectral direction, however, the redshift of a galaxy and the spatial distribution of its Hα are degenerate. As a result, the uncertainty in the spectral direction of the Hα maps is $\sim$0.5 pixels (see Brammer et al. 2012b).

To simultaneously address these problems, we apply an asymmetric double pacman mask to the Hα maps. This mask is shown applied to the stack in Figure 4. The mask serves three purposes. First, it masks the [S II] emission, which otherwise could masquerade as Hα flux at large radii. Second, it mitigates the effect of the redshift–morphology degeneracy by removing the parts of the Hα distribution that would be most affected. Third, it reduces the impact of imperfect stellar continuum

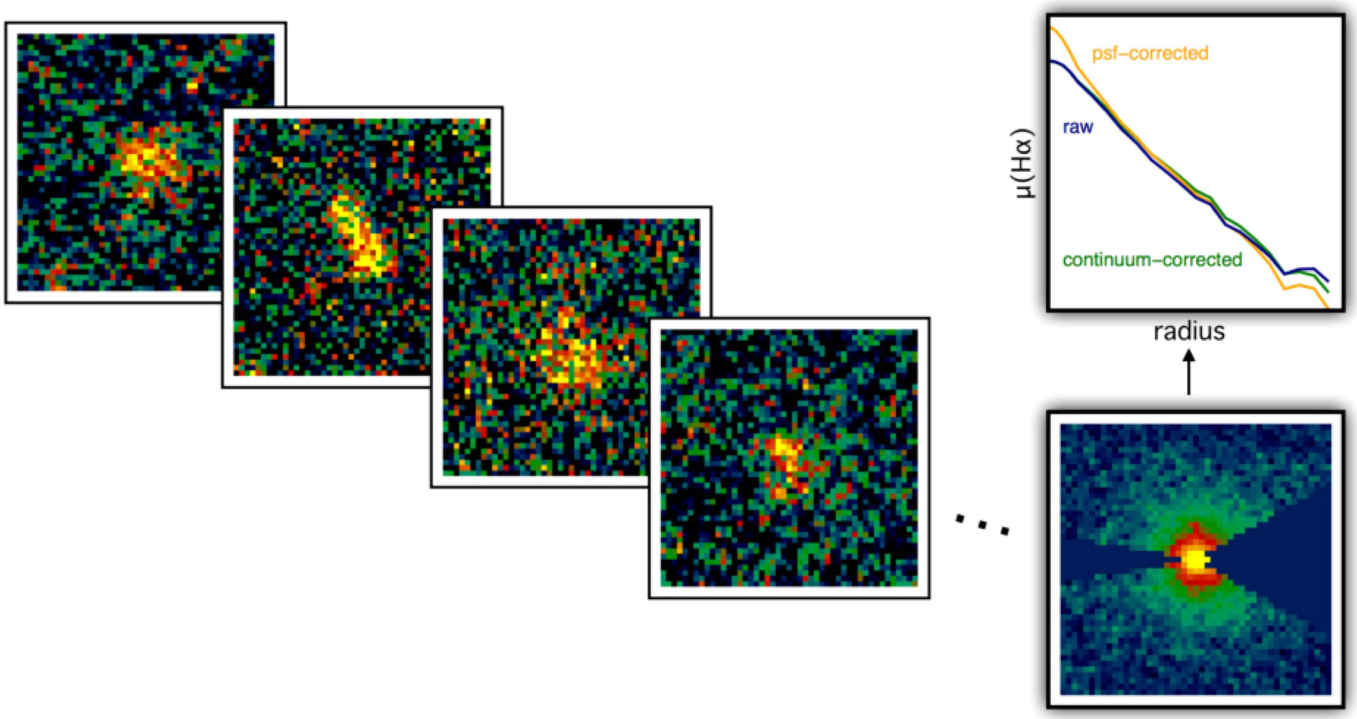

Figure 4. Illustration of the creation of an Hα image stack and the derivation of radial profiles. The panels on the left show four of the 377 Hα maps that are summed to create the stack on the right. The stack is masked with the "double pacman" mask shown, in order to mitigate the effects of redshift uncertainties and [S II] $\lambda\lambda$6716, 6731 (see Section 3.3). The surface brightness profiles derived from this stack are shown above it. The raw profile is shown in black. The profile corrected for residual continuum is shown in green, and the profile corrected for the effects of the PSF is shown in orange.

subtraction by masking the portion of the spectrum that would be most afflicted. The first of these issues only requires a mask redward of Hα. The other two, however, require masking both redward and blueward of Hα.

A mask was also created for each galaxy's $H_{\rm F140W}$ image to cover pixels that are potentially affected by neighboring objects. This mask was constructed from the 3D-*HST* photometric data products. SExtractor was run on the combined $J_{F125W}/H_{F140W}/H_{F160W}$ detection image (see Skelton et al. 2014). Using the SExtractor segmentation map, we flagged all pixels in a postage stamp belonging to other objects and masked them. For both Hα and $H_{\rm F140W}$ a bad pixel mask is created for known bad or missing pixels as determined from the data quality extensions of the fits files.

The final mask for each Hα image is composed of the union of three separate masks: (1) the bad pixel mask, (2) the asymmetric double pacman mask, and (3) the contamination mask (see previous section). A final $H_{\rm F140W}$ mask is made from the combination of two separate masks: (1) the bad pixel mask and (2) the neighbor mask. The Hα and $H_{\rm F140W}$ images are multiplied by these masks before they are summed. Summing the masks creates what is effectively a weight map for the stacks. The raw stacks are divided by this weight map to create the final exposure-corrected stacked images.

3.4. Surface Brightness Profiles

The stacked Hα image for galaxies with $10^{10} < M_* < 10^{10.5}$ is shown in Figure 4. With hundreds of galaxies, this image is very deep and we can trace the distribution of Hα out to large radii ($\sim$10 kpc). To measure the average radial profiles of the Hα and $H_{\rm F140W}$ emission, we compute the surface brightness as a function of radius by measuring the mean flux in circular apertures. We checked that the total flux in the stacks matched the Hα and $H_{\rm F140W}$ fluxes in our catalogs. We compute error bars on the radial profiles by bootstrap resampling the stacks, and in general, we cut off the profiles when S/N < 2.5. The Hα profile for the example stack is shown in Figure 4. Before moving on to discussing the trends in the observed radial profiles, we note two additional corrections made to them.

First, we correct the continuum model used to create the Hα maps. This continuum model goes out to the edge of the segmentation map of each galaxy, which typically encompasses $\gtrsim$95% of the light. We subtract the remaining continuum flux by correcting the continuum model to have the same spatial distribution as the broadband light. The $H_{\rm F140W}$ filter covers the same wavelength range as the G141 grism. Therefore, the radial distribution of $H_{\rm F140W}$ emission reflects the true radial distribution of continuum emission. We derive a correction factor to the continuum model of each stack by fitting a second-degree polynomial to the radial ratio of the $H_{\rm F140W}$ stack to the stacked continuum model. This continuum correction is $<$20% at all radii in the profiles shown here.

Second, we correct the radial profiles for the effect of the PSF. Compared to typical ground-based observations, our space-based PSF is narrow and relatively stable. We model the PSF using Tiny Tim (Krist 1995) and interlacing the model PSFs in the same way as the data. The FWHM of the interlaced PSF is $0\farcs136$, which corresponds to 1.1 kpc at $z \sim 1$. Although this is small, it has an effect, particularly by blurring the centers of the radial profiles. Images can be corrected using a deconvolution algorithm. However, there are complications with added noise in low-S/N regions, and no algorithm perfectly reconstructs the intrinsic light distribution (see, e.g., van Dokkum et al. 2010). We instead employ the

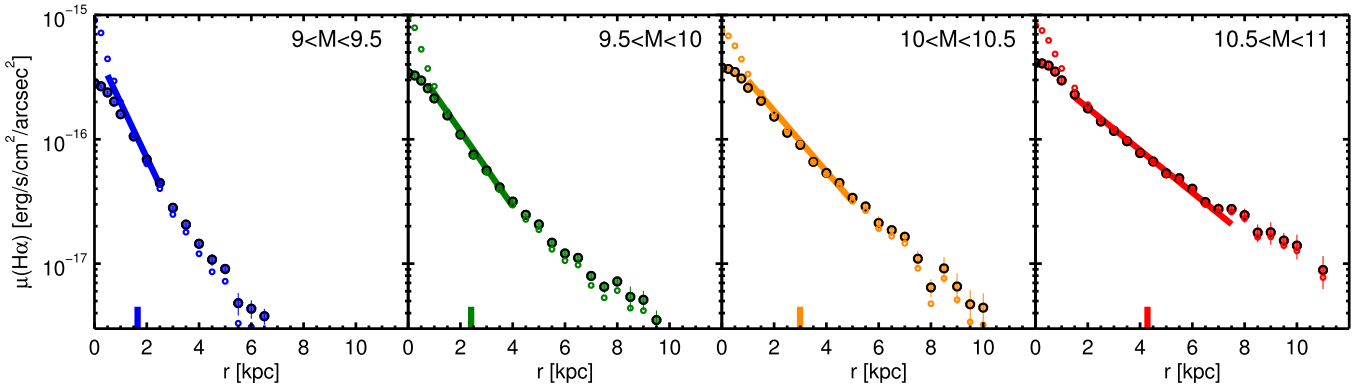

Figure 5. Average radial distribution of Hα emission in galaxies in bins of stellar mass indicated at the top of each panel. The filled circles show the radial profiles measured directly from the stacked Hα images. The open circles show the profiles corrected for the effect of the PSF. The lines show the best-fit exponentials for $0.5r_s < r < 3r_s$ to the PSF-corrected profiles. There appears to be some excess flux over a pure exponential at small and large radii. The short vertical lines show the corresponding Hα effective radii.

algorithmically more straightforward method of Szomoru et al. (2010). This method takes advantage of the GALFIT code, which convolves models with the PSF to fit galaxy light distributions (Peng et al. 2002). We begin by fitting the stacks with Sérsic (1968) models using GALFIT (Peng et al. 2002). These Sérsic fits are quite good, and the images show small residuals. We use these fit parameters to create an unconvolved model of the image stack. To account for deviations from a perfect Sérsic fit, we add the residuals to this unconvolved image stack. Although the residuals are still convolved with the PSF, this method has been shown to reconstruct the true flux distribution even when the galaxies are poorly fit by a Sérsic profile (Szomoru et al. 2010). It is worth noting again that the residuals in these fits are small, so the residual-correction step in this procedure is not critical to the conclusions of this paper.

4. THE DISTRIBUTION OF Hα AS A FUNCTION OF STELLAR MASS AND RADIUS

The structure of galaxies (e.g., Wuyts et al. 2011b; van der Wel et al. 2014b) and their specific star formation rates (sSFRs; e.g., Whitaker et al. 2014) change as a function of stellar mass. This means that both where a galaxy is growing and how rapidly it is growing depend on how much stellar mass it has already assembled. In this section, we investigate where galaxies are building stellar mass by considering the average radial distribution of Hα emission in different mass ranges.

To measure the average spatial distribution of Hα during this epoch from $z = 1.5$ to 0.7, we create mean Hα images by stacking the Hα maps of individual galaxies as described in Section 3.3. The stacking technique employed in this paper serves to increase the S/N, enabling us to trace the profile of Hα to large radii. An obvious disadvantage is that the Hα distribution is known to be different for different galaxies. As an example, the Hα maps of the galaxies shown in Figure 3 are quite diverse, displaying a range of sizes, surface densities, and morphologies. Additionally, star formation in the early universe often appears to be clumpy and stochastic (Elmegreen & Elmegreen 2005; Elmegreen 2009; Förster Schreiber et al. 2011b, Guo et al. 2012). Different regions of galaxies light up with new stars for short periods of time. These clumps, while visually striking, make up a small fraction of the total star formation at any given time. Only 10%–15% of star formation occurs in clumps, while the remaining 85%–90% of star formation occurs in a smooth disk or bulge component (Förster Schreiber et al. 2011b; Wuyts et al. 2012, 2013). Stacking Hα smooths over the short-timescale stochasticity to reveal the time-averaged spatial distribution of star formation.

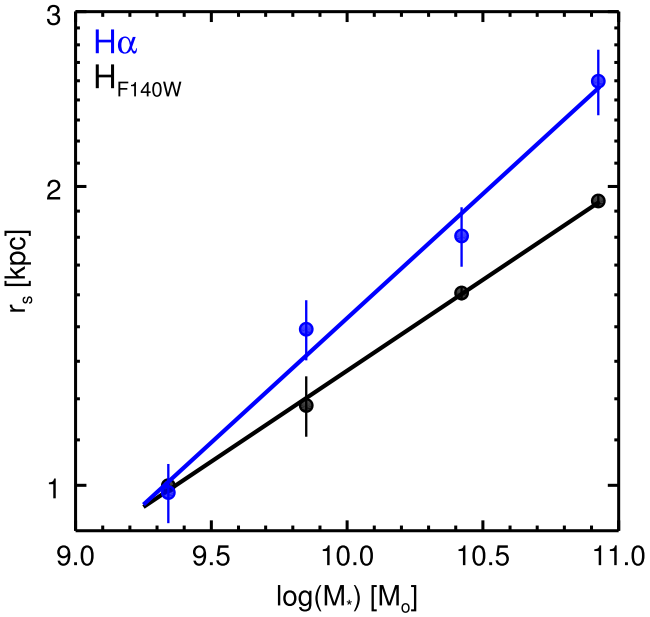

Figure 6. Size–mass relations for Hα ($r_{\rm H\alpha}$–M_*) stellar continuum (r_*–M_*). The size of star-forming disks traced by Hα increases with stellar mass as $r_{\rm H\alpha} \propto M^{0.23}$. At low masses, $r_{\rm H\alpha} \sim r_*$, as mass increases the disk scale length of Hα becomes larger than the stellar continuum emission as $r_{\rm H\alpha} \propto r_* M_*^{0.054}$. Interpreting H$\alpha$ as star formation and stellar continuum as stellar mass, this serves as evidence that, on average, galaxies are growing larger in size due to star formation.

Figure 5 shows the radial surface brightness profiles of Hα as a function of stellar mass. The first and most obvious feature of these profiles is that the Hα is brightest in the center of these galaxies: the radial surface brightness of Hα rises monotonically toward small radii. The average distribution of ionized gas is not centrally depressed or even flat; it is centrally peaked. This shows that there is substantial ongoing star formation in the centers of galaxies at all masses at $z \sim 1$.

With regard to profile shape, in log(flux)-linear(radius) space, these profiles appear to be nearly linear, indicating that they are mostly exponential. There is a slight excess at small and large radii compared to an exponential profile. However,

Table 2
Structural Parameters

	Hα			H_{F140W}		
$\log(M_*)$	r_s	r_e	n	r_s	r_e	n
$9.0 < \log(M_*) < 9.5$	0.98 ± 0.05	1.77 ± 0.11	1.83 ± 0.15	1.00 ± 0.01	1.85 ± 0.02	1.90 ± 0.03
$9.5 < \log(M_*) < 10.0$	1.44 ± 0.03	2.91 ± 0.17	1.98 ± 0.16	1.20 ± 0.06	2.38 ± 0.03	1.89 ± 0.03
$10.0 < \log(M_*) < 10.5$	1.78 ± 0.09	3.10 ± 0.20	1.47 ± 0.10	1.56 ± 0.02	2.97 ± 0.09	1.86 ± 0.03
$10.5 < \log(M_*) < 11.0$	2.55 ± 0.14	5.34 ± 0.80	1.90 ± 0.20	1.93 ± 0.02	3.73 ± 0.10	2.24 ± 0.10

Note. Disk scale length and effective radius in kpc and Sérsic index for Hα and H_{F140W} as a function of stellar mass. For an exponential disk ($n = 1$), $r_e = 1.678 r_s$.

the profile shape is dependent on the stacking methodology: if the profiles are deprojected and normalized by their effective radius (as derived from the H_{F140W} data), they are closer to exponential (see Appendix). We do not use these normalized profiles as the default in the analysis, as it is difficult to account for the effects of the PSF.

We quantify the size of the ionized gas distribution in two ways: fitting exponential profiles and Sérsic models. For simplicity, we measure the disk scale lengths ($\equiv r_s$) of the ionized gas by fitting the profiles with an exponential between $0.5r_s < r < 3r_s$. These fits are shown in Figure 5. It is clear that over the region $0.5r_s < r < 3r_s$ the Hα distribution is reasonably well approximated by an exponential. Out to $5r_s$, ∼90% of the Hα can be accounted for by this single exponential disk fit. This implies that most of the Hα lies in a disk.

The scale length of the exponential disk fits increases with mass from 1.3 kpc for $9.0 < M_* < 9.5$ to 2.6 kpc for $10.5 < M_* < 11.0$. With $r_e = 1.678 r_s$, this corresponds to effective (half-light) radii of 2.2 and 4.4 kpc, respectively. We fit the size–mass relation of the ionized gas disks ($r_{H\alpha}$–M_*) with

$$r_{H\alpha}(m_*) = 1.5 m_*^{0.25}, \quad (2)$$

where $m_* = M_*/10^{10}\,M_\odot$. Fitting the H_{F140W} surface brightness profiles in the same way shows the exponential disk scale lengths of the stellar continuum emission versus the ionized gas. We parameterize this comparison in terms of the stellar continuum size:

$$r_*(m_*) = 1.3 m_*^{0.18} \quad (3)$$

$$r_{H\alpha}(m_*, r_*) = 1.1\, r_*\, (m_*^{0.054}). \quad (4)$$

For $10^9\,M_\odot < M_* < 10^{9.5}\,M_\odot$, the Hα emission has the same disk scale length as the H_{F140W} emission. This suggests that the Hα emission closely follows the H_{F140W} emission (or possibly the other way around). At stellar masses $M_* > 10^{9.5}$ the scale length of the Hα emission is larger than the H_{F140W}. As mass increases, the Hα grows increasingly more extended and does not follow the H_{F140W} emission as closely. The size–mass relations for Hα and H_{F140W} are shown in Figure 6.

The ionized gas distributions can also be parameterized with Sérsic profiles. We fit the observed, PSF-convolved stacks with Sérsic models using GALFIT as described in the previous section. The Sérsic index of each, which reflects the degree of curvature of the profile, is $1 < n < 2$ for all mass bins, demonstrating that they are always disk dominated. The Sérsic indices and sizes measured with GALFIT are listed in Table 2. The sizes measured with GALFIT are similar to those measured using exponential disk fits and exhibit the same qualitative trends.

While the bootstrap error bars for each individual method are very small, 2%–4%, different methodologies result in systematically different size measurements. We derive our default sizes by fitting exponentials to the $0.5r_s < r < 3r_s$ region of PSF-corrected profiles. Fit the same way, sizes are 10%–20% larger when profiles are not corrected for the PSF. Adopting slightly different fitting regions can also change the sizes by 10%–20%. The GALFIT sizes are 3%–15% larger. With all methods the trends described remain qualitatively the same. That is, the effective radius of the Hα emission is always greater than or equal to the effective radius of the H_{F140W}, and both increase with stellar mass.

The comparison between the radial distribution of Hα and H_{F140W} can be seen explicitly in their quotient, the radial Hα equivalent width (EW(Hα)) profile (Figure 7), indicating where the Hα emission is elevated and depressed relative to the H_{F140W} emission. The first and most obvious feature is that the normalization of equivalent width profiles decreases with increasing stellar mass, consistent with spatially integrated results (Fumagalli et al. 2013) and the fact that sSFR declines with stellar mass (e.g., Whitaker et al. 2014). Additionally, below a stellar mass of $\log(M)_* < 9.5$, the equivalent width profile is flat, at least on the scales of $\geqslant$1 kpc resolved by our data. These galaxies are growing rapidly across their disks. In addition to the overall normalization of the EW decreasing, as stellar mass increases, the shape of the EW profile changes, its slope growing steeper. For $9.5 < \log(M_*) < 10.0$, EW(Hα) rises by a factor of ∼1.3 from the center to $2r_e$; for $10.5 < \log(M_*) < 11.0$, it rises by $\gtrsim$3. At low masses, the entire disk is illuminated with new stars; at higher masses, the Hα is somewhat centrally depressed relative to the stellar continuum emission. Consistent with the measured size trends, the radial EW(Hα) profiles show that Hα has a similar distribution to the stellar continuum emission for $9.0 < \log(M_*) < 9.5$; as mass increases, Hα becomes more extended and less centrally concentrated than the stellar continuum emission.

Interpreting Hα as star formation and H_{F140W} as stellar mass implies that star formation during the epoch $0.7 < z < 1.5$ is building galaxies from the inside out, as discussed in Section 7.3.

5. THE RADIAL DISTRIBUTION OF Hα ACROSS THE STAR-FORMING SEQUENCE

In the previous section, we showed how the radial distribution of star formation depends on the stellar mass of a galaxy. Here we show how it depends on the total SFR at fixed mass. In other words, we show how it depends on a galaxy's position in the SFR–M_* plane with respect to the star-forming

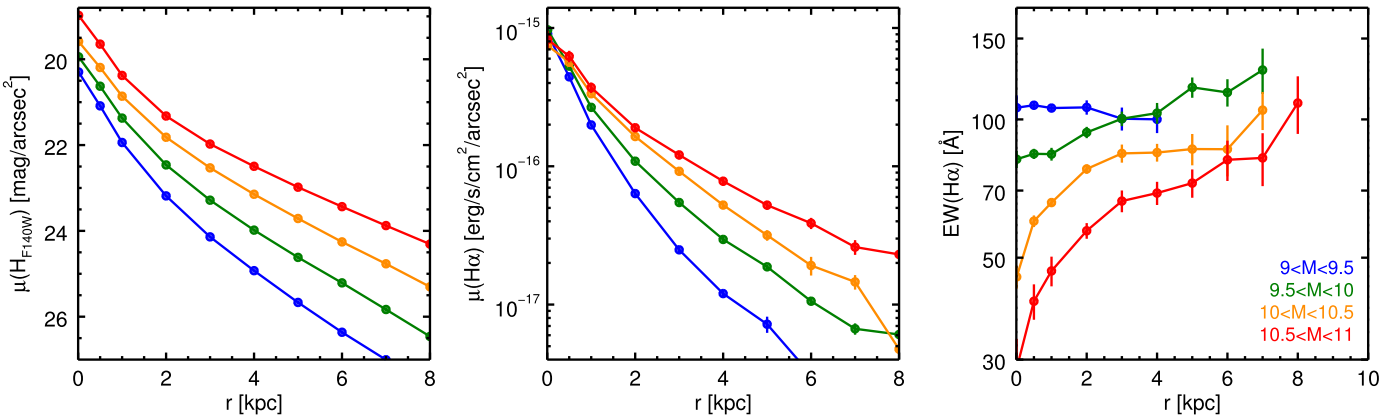

Figure 7. Average radial surface brightness profiles of H_{F140W} (left), Hα (center), and average radial Hα equivalent width profile (EW(Hα)) (right) in galaxies as a function of stellar mass. The radial EW(Hα) profile is the quotient of the Hα and stellar continuum profiles, providing a comparison between the spatial distribution of Hα and stellar continuum emission. At low masses the EW(Hα) profile is flat. As mass increases, EW(Hα) rises increasingly steeply from the center, showing, in agreement with the larger disk scale lengths of Figure 6, that the Hα has a more extended distribution than the existing stellar continuum emission.

MS. The star-forming "MS" is an observed locus of points in the SFR–M_* plane (Brinchmann et al. 2004; Daddi et al. 2007; Elbaz et al. 2007; Noeske et al. 2007; Salim et al. 2007; Zheng et al. 2007; Damen et al. 2009; González et al. 2010; Magdis et al. 2010; Karim et al. 2011; Huang et al. 2012; Whitaker et al. 2012, 2014).

5.1. Definition of the Star-forming Main Sequence

We define the star-forming sequence according to the results of Whitaker et al. (2014), interpolated to $z = 1$. As described in Section 2.2, we use SFR(UV+IR) to place galaxies in the SFR–M_* plane, but the results presented here are similar if SFR (Hα) or SFR(Hα + IR) is used instead. The slope of the relation between SFR and M_* decreases with M_*, as predicted from galaxy growth rates derived from the evolution of the stellar mass function (Leja et al. 2015), reflecting the decreased efficiency of stellar mass growth at low and high masses. Whitaker et al. (2014) find that the observed scatter is a constant $\sigma = 0.34$ dex with both redshift and M_*.

We investigate where "normal" star-forming galaxies were forming their stars at this epoch by determining the radial distribution of Hα in galaxies on the MS. We elucidate how star formation is enhanced and suppressed in galaxies by determining where star formation is "added" in galaxies above the MS and "subtracted" in galaxies below the MS. To determine where star formation is occurring in galaxies in these different regions of the SFR–M_* plane, we stack Hα maps as a function of mass and SFR. We define the MS as galaxies with SFRs $\pm 1.2\sigma = \pm 0.4$ dex from the Whitaker et al. (2014) MS line at $z \sim 1$. Specifically, we consider galaxies "below," "on," or "above" the star-forming MS to be the regions $[-0.8, -0.4]$ dex, $[-0.4, +0.4]$ dex, or $[+0.4, +1.2]$ dex with respect to the MS line in the SFR–M_* plane. To define these regions consistently, we normalize the SFRs of all galaxies to $z \sim 1$ using the redshift evolution of the normalization of the star-forming sequence from Whitaker et al. (2012). These definitions are shown pictorially by Figure 8 in red, black, and blue, respectively. We imposed the +1.2 dex upper limit above the MS so that the stacks would not be dominated by a single, very bright galaxy. We impose the −0.8 dex due to the Hα flux-driven completeness limit. Figure 8 also shows which galaxies were actually used in the stacks. Our broadband magnitude extraction limit and Hα flux limit manifest

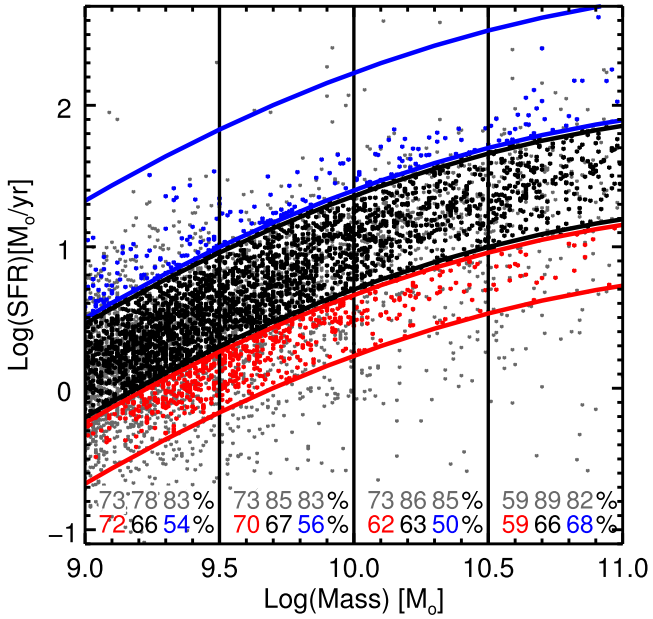

Figure 8. We investigate the spatial distribution of star formation in galaxies across the SFR–M_* plane. To do this, we stack the Hα maps of galaxies on the star-forming MS (black) and compare to the spatial distribution of Hα in galaxies above (blue) and below (red) the MS. The parent sample is shown in gray. The fraction of the total parent sample above the extraction magnitude limit is listed at the bottom in gray. As expected, we are significantly less complete at low masses, below the MS. About one-third of selected galaxies are thrown out of the stacks due to contamination of their spectra by other sources in the field. Of the galaxies above the extraction limit, the fractions remaining as part of the final selection are listed and shown in blue, black, and red, respectively.

themselves as incompleteness primarily at low masses and SFRs as reflected in the gray numbers and filled symbols.

We adopted this $\pm 1.2\sigma$ definition of the MS to enable us to probe the top and bottom 10% of star formers and ferret out differences between galaxies growing very rapidly, those growing very slowly, and those growing relatively normally. According to our definition ($\pm 1.2\sigma$), the "MS" accounts for the vast majority of galaxy growth. It encompasses 80% of *UVJ* star-forming galaxies and 76% of star formation. The star-forming MS is defined by the running median SFR of galaxies

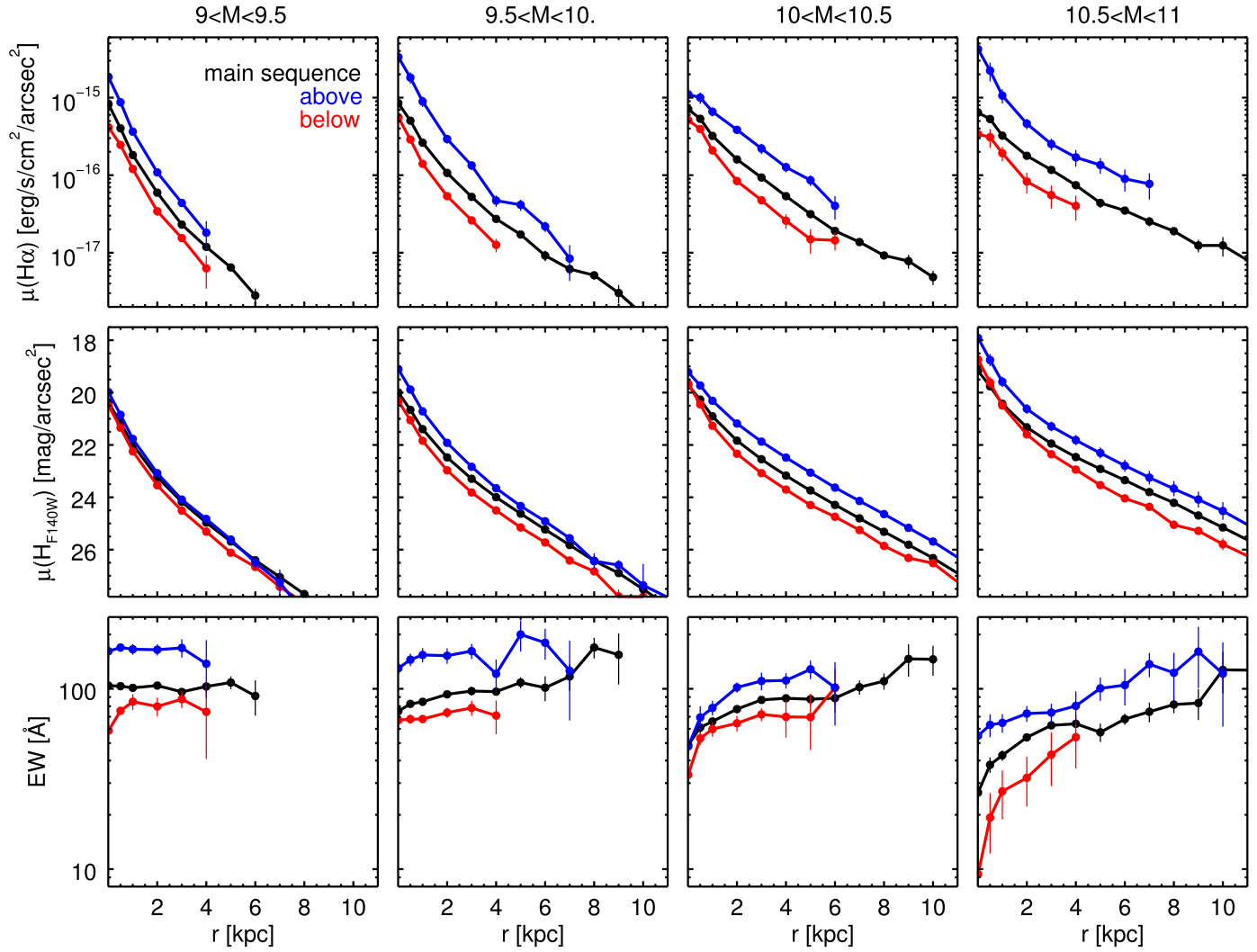

Figure 9. Radial surface brightness profiles of Hα, $H_{\rm F140W}$, and their ratio EW(Hα) as a function of M_* and SFR. The colors delineate position with respect to the star-forming "MS": above (blue), on (black), and below (red). Above the star-forming MS, the Hα (as well as the $H_{\rm F140W}$ and EW(Hα)) is elevated at all radii. Below the star-forming MS, the Hα is depressed at all radii. The average radial profiles are always centrally peaked in Hα and never centrally peaked in EW(Hα).

as a function of mass. The definition is nearly identical when the mode is used instead, indicating that it defines the most common rate of growth. While we left 20% of star-forming galaxies to probe the extremes of rapid and slow growth, only 7% of these galaxies live above the MS and nearly double that, 13%, live below it. This is a manifestation of the fact that the distribution of SFRs at a given mass is skewed toward low SFRs. Counting galaxies, however, understates the importance of galaxies above the MS to galaxy evolution because they are building stellar mass so rapidly. Considering instead the contribution to the total star formation budget at this epoch, galaxies above the MS account for >20% of star formation, while galaxies below the MS only account for <3%.

5.2. Spatially Coherent Star Formation

One of the primary results of this paper is shown in Figure 9: the radial distribution of Hα on, above, and below the star-forming MS. Above the MS, Hα is elevated at all radii. Below the MS, Hα is depressed at all radii. The profiles are remarkably similar above, on, and below the MS—a phenomenon that can be referred to as "coherent star formation," in the sense that the offsets in the SFR are spatially coherent.

We quantify this spatially coherent star formation in the following way. First, we determine the overall offset of the Hα flux above and below the MS. To do this, we divide the Hα surface brightness profiles above and below the MS by their MS counterparts. These MS-normalized radial profiles are shown in Figure 10. The mean offset of these profiles is roughly a factor of 2 (0.3 dex).

Next, we compare the offset from the MS at small radii to the offset at large radii. The ratio of the offset between $1.5 < r < 3$ and $3 < r < 4.5$ is ~1 for all mass bins above and below the star-forming MS. Star formation is spatially coherent: the offset is roughly a factor of 2 and nearly independent of radius. The mean offsets, as well as the ratio of the offsets at large and small radii, are listed in Table 3. Above the MS at the highest masses where we have the S/N to trace the Hα to large radii, we can see that the Hα remains enhanced by a factor of $\gtrsim$2 even beyond 10 kpc. The most robust conclusion we can draw from the offsets in the radial profiles of Hα is that star formation from ~1.5 to 4.5 kpc is enhanced coherently in galaxies above the MS

and suppressed coherently in galaxies below the MS (but see Section 7.4 for further discussion).

We emphasize that the SFRs used in this paper were derived from UV+IR emission. These SFR indicators are measured independently from the Hα flux. Thus, it is not a priori clear that the Hα emission is enhanced or depressed for galaxies above or below the star-forming MS as derived from the UV +IR emission. The fact that it is implies that the scatter in the star-forming sequence is real and caused by variations in the SFR (see Section 7.4).

We use SFR(UV+IR) instead of SFR(Hα) as the default integrated SFR measure for placing galaxies in the SFR–M_* plane. We chose this method to minimize the effects of dust on systematic structural measurements of Hα above and below the MS. We compare the MS offset in the Hα surface brightness profiles when sorting by SFR(Hα) instead of SFR(IR+UV). Unsurprisingly, we find that the offset between the Hα surface brightness profiles is larger: it increases from a factor of ∼2 to a factor of ∼3. Crucially, what remains robust is that the ratio of the offset between $1.5 < r < 3$ and $3 < r < 4.5$ is ∼1 for all mass bins above and below the star-forming MS. In sum, when using a different star formation indicator to define the MS, star formation remains spatially coherent, but there is a larger offset between above, on, and below the star-forming sequence.

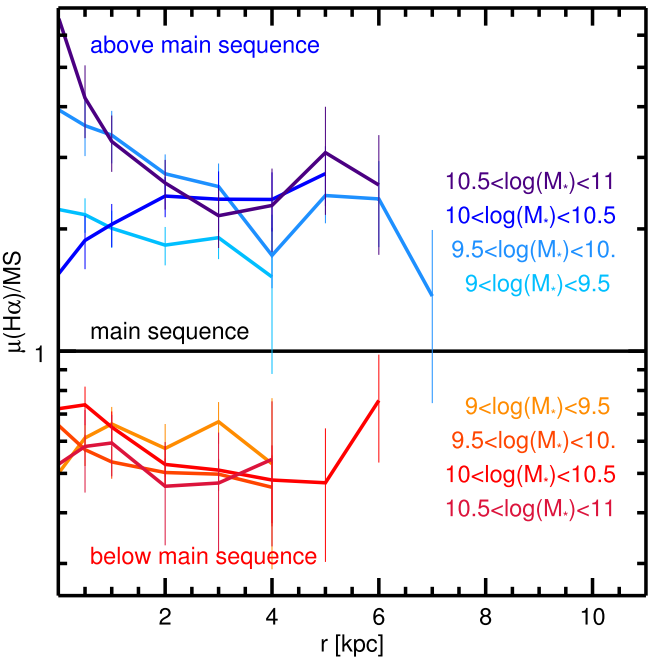

Figure 10. Radial profiles of Hα as a function of mass normalized by the MS radial profile. Above the star-forming MS, the Hα is elevated at all radii (blue hues). Below the star-forming MS, the Hα is depressed at all radii (red hues).

5.3. Hα Sizes as a Function of Star Formation Rate and Mass

Spatially coherent star formation is also manifest in the average structural parameters of the Hα emission above and below the MS. Figure 11 and Table 4 present disk scale lengths of the Hα and stellar continuum emission as a function of mass on, above, and below the MS. We note that the error bars include both the bootstrap errors and sizes determined from stacking based on total SFR(Hα) instead of the default SFR (UV+IR).

We find that systematic trends in the disk scale length of Hα are stronger with stellar mass than with SFR at fixed mass. That is, the average disk scale length of Hα emission is driven more by stellar mass than by whether a galaxy is above or below the MS. At fixed mass, the total SFR does not dramatically impact the disk scale length of the Hα emission, a manifestation of spatially coherent star formation.

We fit the size–mass (r_s–M_*) relation for disk scale lengths in Hα and $H_{\rm F140W}$ emission on, above, and below the star-forming MS. As in Section 4, we fit a linear relation between $\log(r_s)$ and $\log(M_*)$:

$$a + \log(r_s) = b^*(\log M_* - 10.0). \quad (5)$$

Values for b and c are listed in Table 5. The slope and normalization of the r_s–M_* relation for Hα on, above, and below are consistent within the error bars. There is no statistically significant offset in the r_s(Hα)–M_* relation due to total star formation: star formation is spatially coherent.

5.4. Stellar Continuum and Equivalent Width

In the middle panels of Figure 9 we show the radial profiles of $H_{\rm F140W}$ emission as a function of M_* above, on, and below the star-forming MS. As expected, we find that with increasing stellar mass, the surface brightness profiles of $H_{\rm F140W}$ grow both steeper and more spatially extended. At high masses, we find that both above and below the MS, the $H_{\rm F140W}$ is somewhat more centrally concentrated than on the MS (consistent with Wuyts et al. 2011b; Lang et al. 2014; Whitaker et al. 2015), possibly indicating more dominant bulges. These trends are less obvious at lower masses. Furthermore, as one would expect, the mass-to-light ratio decreases with sSFR because young stars are brighter than old stars. Therefore, at fixed mass, galaxies above the MS have brighter $H_{\rm F140W}$ stellar continuum emission, and galaxies below the MS have fainter $H_{\rm F140W}$ emission.

Table 3
Hα Flux Offset above and below Main Sequence

	Offset[a]		Inner/Outer[b]	
$\log(M_*)$	Below	Above	Below	above
$9.0 < \log(M_*) < 9.5$	−0.23 ± 0.07	0.26 ± 0.05	0.90 ± 0.15	0.99 ± 0.12
$9.5 < \log(M_*) < 10.0$	−0.30 ± 0.04	0.41 ± 0.06	1.15 ± 0.22	1.39 ± 0.24
$10.0 < \log(M_*) < 10.5$	−0.29 ± 0.04	0.37 ± 0.05	1.10 ± 0.20	0.99 ± 0.11
$10.5 < \log(M_*) < 11.0$	−0.30 ± 0.11	0.39 ± 0.07	1.01 ± 0.16	1.11 ± 0.13

Notes.
[a] Overall offset of the Hα flux below and above the MS in dex for 1.5 kpc $< r <$ 4.5 kpc.
[b] Ratio of offset at small radii ($1.5 < r < 3$) to offset at large radii ($3 < r < 4.5$). This ratio is ∼1, indicating that star formation is spatially coherent. See Section 5.2.

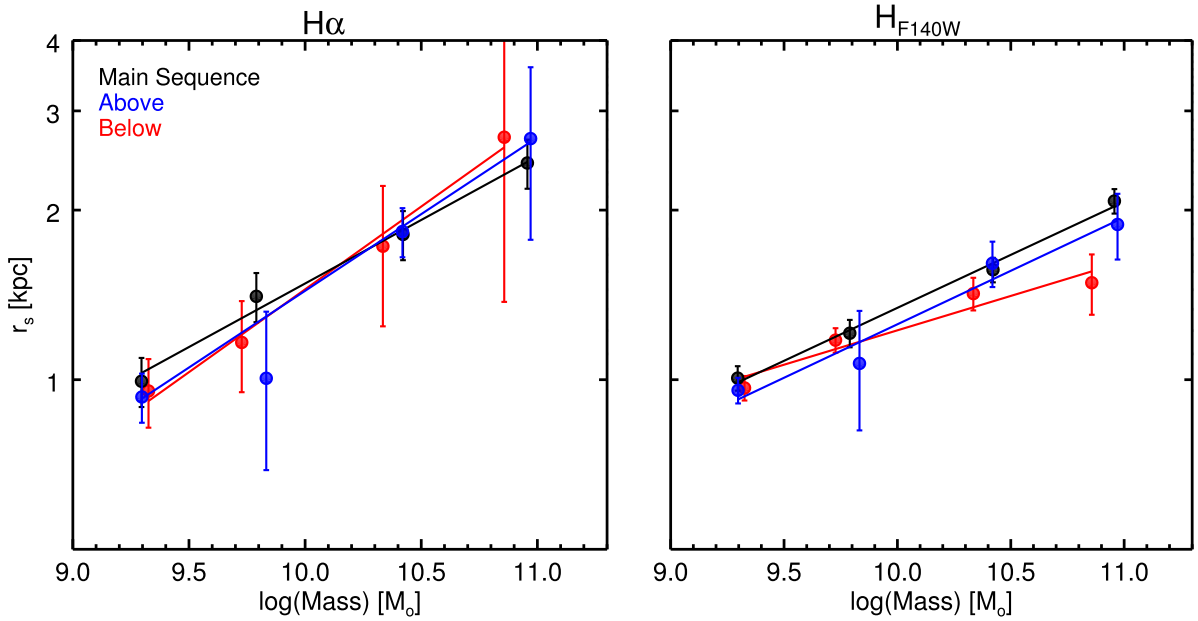

Figure 11. Size–mass relation for Hα and $H_{\rm F140W}$ on, above, and below the star-forming sequence. The average disk scale length of Hα emission is driven more by stellar mass than whether a galaxy is above or below the MS, suggesting that star formation is spatially coherent. Both the slope and normalization of the r_s(Hα)–M_* are higher than those of the $r_s(H_{F140W})$–M_* relation. The disk scale lengths of $H_{\rm F140W}$ also appear to be driven more by mass than by whether a galaxy is above or below the MS except at high masses below the MS, where the $H_{\rm F140W}$ is significantly more compact.

Table 4
Disk Scale Lengths of Hα and Stellar Continuum Emission below, on, and above the Star-forming Main Sequence

	r_s(Hα) [kpc]			$r_s(H_{\rm F140W})$ [kpc]		
log(M_*)	Below	MS	Above	Below	MS	Above
$9.0 < \log(M_*) < 9.5$	0.95 ± 0.18	0.99 ± 0.10	0.93 ± 0.09	0.97 ± 0.05	1.01 ± 0.05	0.96 ± 0.05
$9.5 < \log(M_*) < 10.0$	1.16 ± 0.21	1.41 ± 0.14	1.01 ± 0.31	1.18 ± 0.06	1.21 ± 0.07	1.07 ± 0.26
$10.0 < \log(M_*) < 10.5$	1.73 ± 0.48	1.81 ± 0.18	1.83 ± 0.18	1.42 ± 0.09	1.57 ± 0.08	1.61 ± 0.15
$10.5 < \log(M_*) < 11.0$	2.69 ± 1.32	2.42 ± 0.24	2.68 ± 0.91	1.49 ± 0.18	2.08 ± 0.10	1.89 ± 0.25

Table 5
r_s–M_* Relation Fit Parameters for Hα and $H_{\rm F140W}$ above, on, and below the Main Sequence

	Hα		$H_{\rm F140W}$	
SFR with respect to MS	a	b	a	b
Above	0.158 ± 0.030	0.272 ± 0.055	0.098 ± 0.010	0.190 ± 0.035
On	0.171 ± 0.008	0.226 ± 0.022	0.128 ± 0.006	0.188 ± 0.011
Below	0.160 ± 0.050	0.294 ± 0.112	0.088 ± 0.005	0.122 ± 0.007

Note. b and c from fit to r_s–M_* relation using: $\log(r_s) = a + b * (\log M_*–10.0)$ (see Section 5.3).

We also measure disk scale lengths and fit size–mass relations for the $H_{\rm F140W}$ above, on, and below the star-forming sequence. These measurements are shown in Figure 11 and listed in Tables 4 and 5. Both the slope and normalization of the $r_s(H_{F140W})$–M_* relation are lower than the r_s(Hα)–M_* relation. Above, on, and below the star-forming sequence the Hα has larger disk scale lengths than the stellar continuum emission. Interestingly, the slope of the $r_s(H_{F140W})$–M_* for galaxies below the MS is significantly shallower than for galaxies on or above it. High-mass galaxies below the MS have systematically smaller sizes.

In the bottom panels of Figure 9 we show the radial EW(Hα) profiles. The most obvious feature of these profiles is that EW(Hα) is *never* centrally peaked. EW(Hα) is always flat or centrally depressed, indicating that the Hα is always equally or less centrally concentrated than the $H_{\rm F140W}$ emission. Above the MS, the EW(Hα) is elevated at all radii. Below the MS, the EW(Hα) is depressed at most radii. These trends are discussed more extensively in Sections 7.4–5, where we convert the EW(Hα) profiles to sSFR profiles.

6. EFFECTS OF ORIENTATION

In the previous sections we analyzed average images and radial profiles of Hα emission with galaxies stacked as they were oriented on the detector. This methodology has the advantage that it allows for better control of systematics. In particular, we can effectively subtract the continuum out to large radii as we can use the radial distribution of the $H_{\rm F140W}$ flux to correct for the $\leqslant$5% of flux missing from the continuum

models. A galaxy's position angle on the detector, however, is arbitrary and has no physical meaning.

Here we present stacks of galaxies rotated to be aligned along the major axis, as measured from the continuum emission. This is an important test of the idea that the Hα emission originates in disks that are aligned with the stellar distribution: in that case, these rotated Hα stacks should have similar axis ratios to the rotated $H_{\rm F140W}$ stacks. We divide the galaxies into the same mass bins as in the previous sections and compare the most face-on versus the most edge-on galaxies. The position angle and projected axis ratio ($q = B/A$) of each galaxy are measured from its $H_{\rm F140W}$ image using GALFIT (Peng et al. 2002). We rotate the $H_{\rm F140W}$ and Hα images according to their $H_{\rm F140W}$ position angle to align them along the major axis. In each mass bin, we then create face- and edge-on stacks from the galaxies with the highest and lowest 20% in projected axis ratio, respectively.

The distribution of projected axis ratios is expected to be broad if most galaxies are disk dominated (see, e.g., van der Wel et al. 2014a). If we interpret the galaxy images as disks under different orientations, we would expect the stacks of galaxies with the highest 20% of projected axis ratios to have an average axis ratio of ∼0.9 and the stacks of galaxies with the lowest 20% of projected axis ratios to be flattened with average axis ratios of ∼0.3 (see van der Wel et al. 2014a). As shown in Figure 12, the rotated $H_{\rm F140W}$ stacks are consistent with this expectation. Furthermore, the rotated Hα stacks are qualitatively very similar to the rotated $H_{\rm F140W}$ stacks, which means that the Hα emission is aligned with that of the stars.

For the edge-on stacks, we measure the flattening of the Hα emission and compare it to that of the $H_{\rm F140W}$ emission. In the four mass bins, from low mass to high mass, we find $q({\rm H}\alpha) = [0.29 \pm 0.02, 0.32 \pm 0.03, 0.31 \pm 0.02, 0.37 \pm 0.02]$ and $q(H_{\rm F140W}) = [0.28 \pm 0.01, \quad 0.27 \pm 0.01, \quad 0.29 \pm 0.01, 0.34 \pm 0.01]$, respectively, where the errors are determined from bootstrap resampling. We find that the average axis ratio of $H_{\rm F140W}$ emission is $q(H_{F140W}) = 0.295 \pm 0.005$ and $q({\rm H}\alpha) = 0.323 \pm 0.011$. We conclude that the H$\alpha$ is slightly less flattened than the $H_{\rm F140W}$ emission, but the difference is only marginally significant.

There are physical reasons why Hα can have an intrinsically larger scale height than the $H_{\rm F140W}$ emission. Given that outflows are ubiquitous in the $z \sim 2$ universe (e.g., Shapley et al. 2003; Shapiro et al. 2009; Genzel et al. 2011, 2014b; Kornei et al. 2012; Newman et al. 2012; Förster Schreiber et al. 2014), it is possible that the Hα would have a larger scale height due to winds driving ionized gas out of the plane of the stellar disk. Furthermore, attenuation toward H II regions could be more severe in the midplane of the disk than outside of it. This would result in Hα emission being less concentrated around the plane of the disk, giving a larger scale height. Finally, the gas disks and the stellar disks can be misaligned. The fact that the edge-on Hα and $H_{\rm F140W}$ stacks are so similar shows that all these effects are small.

At a more basic level, an important implication of the similarity of the Hα stacks and the $H_{\rm F140W}$ stacks is that it directly shows that we are not stacking noise peaks. If we were just stacking noise, a stack of galaxies flattened in $H_{\rm F140W}$ would not be flattened in Hα because the noise would not know about the shape of the $H_{\rm F140W}$ emission. It is remarkable that this holds even for the lowest-mass stack, which contains the galaxies with the lowest Hα S/N, as well as the smallest disk scale lengths.

7. DISCUSSION

Thus far, we have only discussed direct observables: $H_{\rm F140W}$ and Hα. In this section we explicitly interpret the radial profiles of Hα as radial profiles of star formation and the radial profiles of $H_{\rm F140W}$ as radial profiles of stellar surface density.

7.1. Interpreting Hα and H$_{F140W}$ as SFR and Mass

In Sections 4 and 5, we showed the radial distribution of Hα, $H_{\rm F140W}$, and EW(Hα). Hα emission is typically used as a tracer of star formation, $H_{\rm F140W}$ (rest-frame optical) emission as a proxy for stellar mass, and EW(Hα) for the sSFR (e.g., Förster Schreiber et al. 2011a; Wuyts et al. 2013; Genzel et al. 2014a; Tacchella et al. 2015a, 2015b). In Figures 13 and 14 we show radial profiles of SFR, M_*, and sSFR derived from the observed Hα, HF140W, and EW(Hα) shown in Figures 7 and 9. If we assume that Hα traces star formation and $H_{\rm F140W}$ traces stellar mass, the profiles can be scaled to these physical quantities using the integrated values. To derive mass surface density profiles, we ignore M/L gradients and apply the integrated $M_*/L_{\rm F140W}$ as a constant scale factor at all radii. Similarly, to derive star formation surface density profile, we ignore radial dust gradients and scale the Hα profiles based on the integrated ${\rm SFR(UV + IR)}/L_{\rm H\alpha}$ ratio. The sSFR profile is then the quotient of the SFR and M_* profiles. However, there are a number of caveats associated with interpreting the $H_{\rm F140W}$, Hα, and EW(Hα) profiles in this manner.

We first assess the assumption that there are no radial gradients in the SFR/Hα ratio. This assumption can be undermined in four ways: dust, AGNs, winds, and metallicity, which have opposing effects. Dust will increase the SFR/Hα ratio by obscuring the ionizing photons from star-forming regions. AGNs, winds, and higher metallicity will reduce the SFR/Hα ratio, as they add ionizing photons that do not trace star formation. These aspects, and hence the extent to which a scaling from Hα to SFR is a good assumption, themselves depend on stellar mass and SFR. Dust attenuation is correlated with stellar mass (e.g., Reddy et al. 2006, 2010; Pannella et al. 2009; Wuyts et al. 2011a; Whitaker et al. 2012; Momcheva et al. 2013). At fixed mass, dust attenuation is also correlated with SFR (Wang & Heckman 1996; Adelberger & Steidel 2000; Hopkins et al. 2001; Reddy et al. 2006, 2010, 2015; Wuyts et al. 2011a; Sobral et al. 2012; Domínguez et al. 2013). Within galaxies, dust attenuation is anticorrelated with radius (e.g., Wuyts et al. 2012), as it depends on the column density. This means that SFR and Hα should trace each other reasonably well for low-mass galaxies with low SFRs, and particularly poorly in the centers of massive, rapidly star-forming galaxies (Nelson et al. 2014; van Dokkum et al. 2015). The same qualitative scalings with mass and star formation likely apply to the likelihood of an AGN being present, outflows, and the contamination of Hα by [N II]. That is, AGNs are most likely to haunt the centers of massive, rapidly star-forming galaxies (e.g., Rosario et al. 2013; Förster Schreiber et al. 2014; Genzel et al. 2014b). [N II]/Hα is most likely to be enhanced above the assumed value in the centers of massive galaxies (as described in Section 3.3). Shocks from winds may contribute to the Hα emission in the central regions, particularly at high masses (Newman et al. 2012; Förster

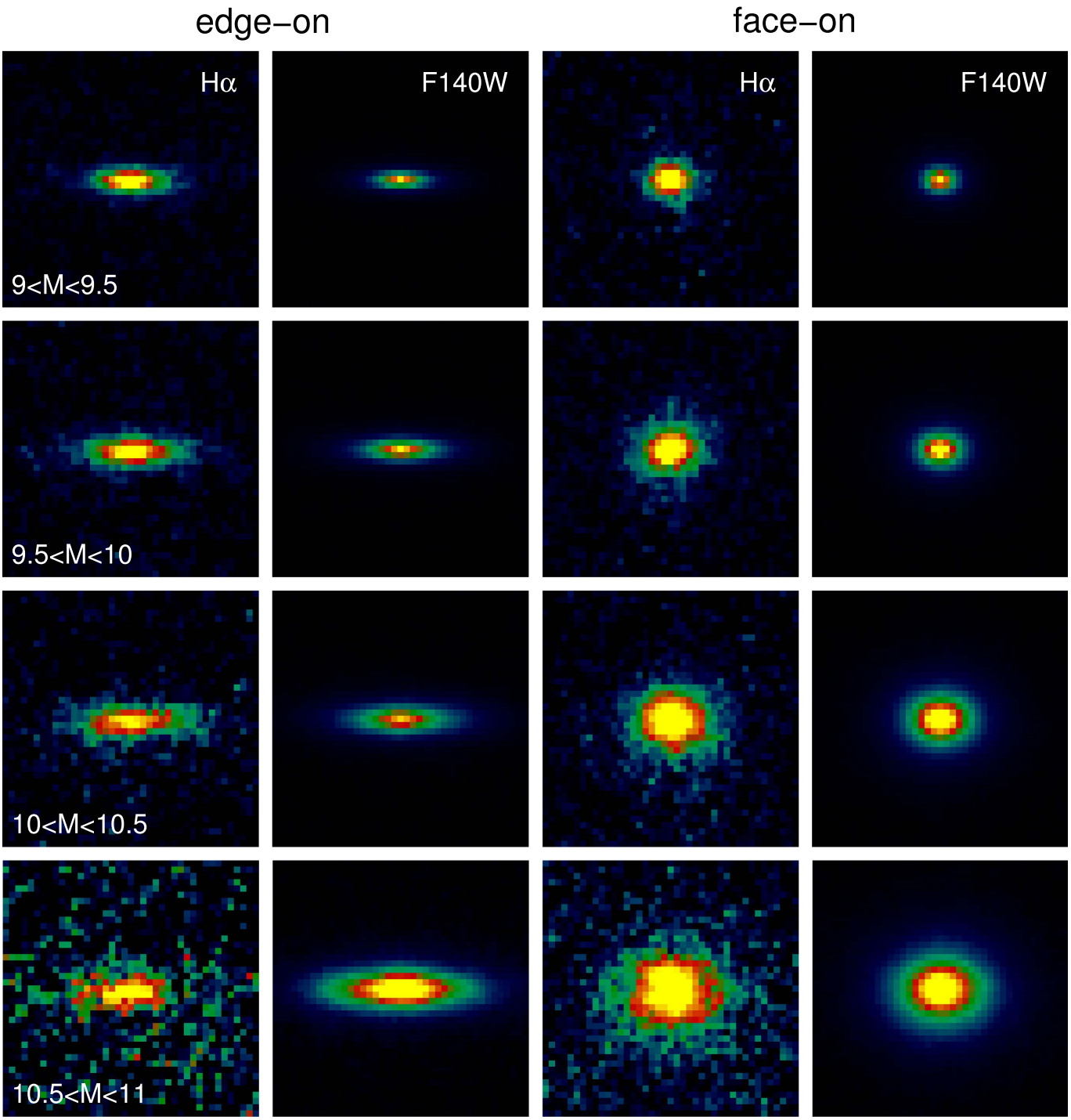

Figure 12. Stacks of galaxies after rotating them so that their major axes are aligned, for the 20% of galaxies with the lowest ellipticities ("face-on") and the 20% of galaxies with the highest ellipticiticies ("edge-on"). The lowest-ellipticity stacks are nearly round, and the highest-ellipticity stacks are highly flattened with $a/b \approx 0.3$, consistent with viewing disks under different projections. The Hα stacks are remarkably similar to the $H_{\rm F140W}$ stacks, demonstrating that the Hα emission is aligned with the $H_{\rm F140W}$ emission at all masses.

Schreiber et al. 2014; Genzel et al. 2014b). The takeaway here is that we are relatively confident interpreting Hα as star formation at low masses, low SFRs, and all profiles outside of the center. We are less confident for the centers of the radial profiles of massive or highly star-forming galaxies.

Next, we assess the assumption that there is no radial gradient in the M/L. Dust and AGNs affect the M/L in the same way as SFR/Hα although less strongly (e.g., Calzetti et al. 2000; Wuyts et al. 2013; Marsan et al. 2015; Reddy et al. 2015). Galaxies growing inside out will also have gradients in their stellar population ages. Since older stellar populations have higher M/L, these age gradients translate into M/L gradients. Age and dust increase $M_*/H_{\rm F140W}$, and AGNs decrease it. Hence, using $H_{\rm F140W}$ as a proxy for M_* is a fairly

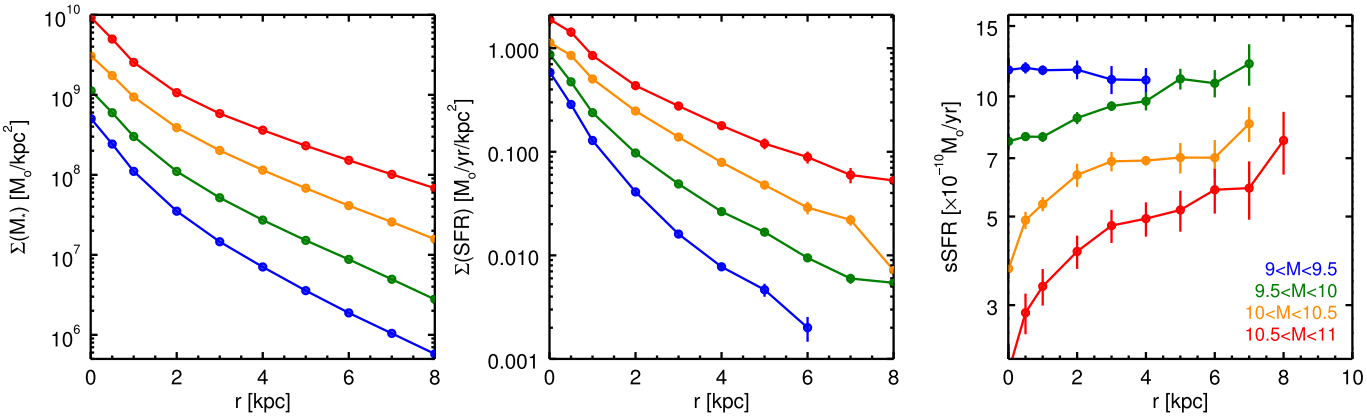

Figure 13. Stellar mass surface density (left), star formation surface density (middle), and sSFR (right) as a function of radius and stellar mass. These profiles were made by scaling the profiles of Hα, $H_{\rm F140W}$, and EW(Hα) in Figure 7 to SFR, M_*, and sSFR. Within galaxies, the sSFR rises radially; the star formation is more extended than the existing stellar mass. This is a direct demonstration that galaxies at this epoch grow inside out.

safe assumption at lower masses where age and dust gradients are small and AGNs are rare. It is somewhat less certain at high masses. We also note that the contribution of the Hα emission to the total $H_{\rm F140W}$ flux is small, ∼5%.

As the EW(Hα) profile is the quotient of the Hα and $H_{\rm F140W}$, interpreting it as a profile of sSFR is accompanied by the amalgam of all of the above uncertainties: dust, age, AGNs, and metallicity. This does not necessarily mean that the sSFR profile is more uncertain than the profiles of star formation and mass, as some effects cancel. In a two-component dust model (e.g., Calzetti et al. 1994; Charlot & Fall 2000), the light from both stars and H II regions is attenuated by diffuse dust in the ISM. The light from the H II regions is attenuated additionally by dust in the undissipated birth clouds. Because the continuum and line emission will be affected equally by the diffuse dust, the EW(Hα) profile will only be affected by the extra attenuation toward the stellar birth clouds, not the totality of the dust column. As a consequence, the effect of dust on the EW(Hα) profiles is mitigated relative to the Hα profiles. The quantity of extra attenuation toward H II regions remains a matter of debate, with estimates ranging from none (Erb et al. 2006b; Reddy et al. 2010) to a factor of 2.3 (Calzetti et al. 2000; Yoshikawa et al. 2010; Wuyts et al. 2013) and many in between (e.g., Förster Schreiber et al. 2009; Mancini et al. 2011; Wuyts et al. 2011a; Kashino et al. 2013). As with the total attenuation, the quantity of extra attenuation toward H II regions appears to increase with M_* and SFR (Price et al. 2014; Reddy et al. 2015). Reddy et al. (2015) find that extra attenuation becomes significant at SF$R \sim 20\ M_\odot\ {\rm yr}^{-1}$. If true, extra extinction should be taken into account for galaxies on the MS at the highest masses and above the MS at $\log(M_*) > 9.5$. The issue should be less acute for galaxies with low masses and SFRs. The only way to definitively resolve this question is to obtain spatially resolved dust maps in the future.

7.2. Star Formation in Disks

We find that Hα emission lies primarily in galactic disks. We showed this with two pieces of evidence. First, as discussed in Section 4, the radial distribution of Hα is nearly exponential with Sérsic indices $1 < n < 2$ typical for galactic disks. Out to $7r_s$, ∼85% of the Hα can be accounted for by a single exponential disk fit. Second, as discussed in Section 6, the average Hα images of galaxies stacked according to their projected axis ratios are consistent with disks under different viewing angles. From the profile shapes and geometries, the picture that emerges is that most of the Hα emission at this time lies in exponential disks.

Assuming that Hα is a good tracer of star formation, the same argument holds for where star formation occurs. The middle panel of Figure 13 shows the radial distribution of SFR as a function of stellar mass derived by scaling the Hα profiles to the total SFR(UV+IR). This means that during the epoch $0.7 < z < 1.5$, most of the star formation in most galaxies occurs in disks.

But not all. The most significant "but" here is dust attenuation. Galaxies with $\log(M_*) > 10$ have ≈2 mag of dust attenuation obscuring the star formation in their centers (Nelson et al. 2016). If we account for this dust attenuation, the star formation in the central $r < 2$ kpc has a distribution that is significantly steeper than exponential. This means that in massive galaxies, in addition to building galactic disks, star formation is also building the stellar mass content of bulges in situ. On the other hand, galaxies with $\log(M_*) < 10$ have little dust attenuation at all radii. This means that their Hα emission is a good tracer of star formation and their star formation really does occur predominately in exponential disks as indicated by the Hα. In sum, we are seeing evidence that in galaxies below $\log(M_*) = 10$, star formation primarily builds disks; in galaxies above $\log(M_*) = 10$, star formation builds both disks and bulges. (These results are described in more detail in Nelson et al. 2016.)

We also note the existence of an Hα excess at large radii; 10% of the total Hα emission is in excess above an exponential at $r > 3r_s$. We do not know the cause of this surplus Hα emission. It could potentially indicate star formation building the stellar halo in situ, excited gas being driven out of galaxies, or the shock heating of the inflowing gas that fuels star formation.

7.3. Inside-out Growth

The star formation surface density (as traced by Hα) is always centrally peaked, but the sSFR (as traced by EW(Hα)) is never centrally peaked. Confirming Nelson et al. (2013), we find that, in general, EW(Hα) is lower in the center than at larger radii. Confirming Nelson et al. (2012), we find that the effective radius of the Hα emission is generally larger than the effective radius of the $H_{\rm F140W}$ emission. This means that the Hα emission is more

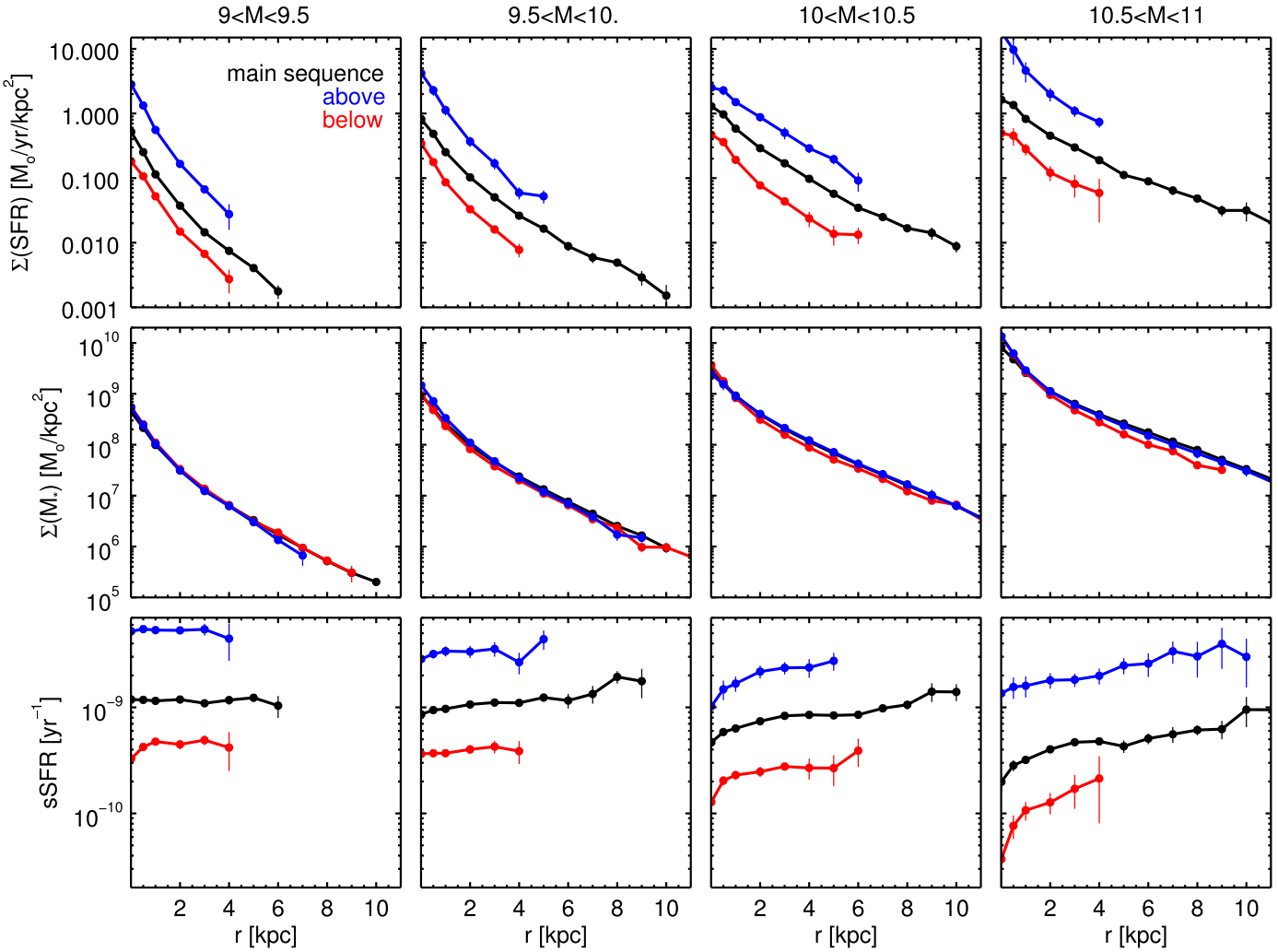

Figure 14. Radial surface brightness profiles of SFR, M_*, and their ratio sSFR as a function of M_* and SFR. The colors delineate position with respect to the star-forming "MS": above (blue), on (black), and below (red). SFR and M_* profiles are Hα and $H_{\rm F140W}$ profiles scaled to the total SFR(UV+IR) and M_* with all the caveats described in Section 7.1. Out to distances as great as 8 kpc from the galactic center, star formation is enhanced in galaxies above and depressed in galaxies below the star-forming MS. This is also true of the sSFR. In general, the radial distribution of M_* is similar on, above, and below the MS on average. It becomes slightly more centrally concentrated in galaxies above and below the MS at the highest masses, as shown in Figure 15. There are two takeaway messages from this figure: (1) the SFR, on average, is always the highest in the centers of galaxies; (2) the radial distribution of star formation depends more strongly on M_* than SFR at fixed mass (a galaxy's position with respect to the MS).

extended and/or less centrally concentrated than the $H_{\rm F140W}$ emission. If Hα traces star formation and $H_{\rm F140W}$ traces stellar mass, these results indicate that galaxies have radial gradients in their sSFRs: the sSFR increases with radius. If the centers are growing more slowly than the outskirts, galaxies will build outward, adding proportionally more stars at larger radii. This suggests that star formation is increasing the size of galaxies. However, galaxies are still building significantly at their centers (probably even more than we see due to the effects of dust), consistent with the fact that size growth due to star formation appears to be fairly weak (van Dokkum et al. 2013; van der Wel et al. 2014b; van Dokkum et al. 2015).

Additionally, there appears to be a trend in $r_s({\rm H}\alpha)/r_s(H_{F140W})$ with mass. Below $3\times10^9\,M_\odot$, the Hα and the $H_{\rm F140W}$ roughly trace each other: the radial EW profile is flat and $r_s({\rm H}\alpha)\sim r_s(H_{F140W})$. As mass increases, H$\alpha$ becomes more extended than the $H_{\rm F140W}$ emission: the EW(Hα) profile is increasingly centrally depressed and $r_s({\rm H}\alpha) > r_s(H_{F140W})$. This reflects the natural expectations of inside-out growth and the shape of the sSFR–M_* relation from both a physical and an observational standpoint.

Observationally, our tracers Hα and $H_{\rm F140W}$ may trace somewhat different things as a function of increasing stellar mass. At the low-mass end, because low-mass galaxies have such high sSFRs, it is possible that the $H_{\rm F140W}$ emission is dominated by light from young stars and is not actually a good tracer of stellar mass. This means that there may in fact be a difference in the disk scale lengths of the stellar mass and star formation, but it is hard to detect because our proxy for M_* is dominated by the youngest stars. At the high-mass end, galaxies have more dust, so star formation could be preferentially obscured at small radii. Consequently, the Hα could appear to be less centrally concentrated than the star formation is in reality, making the inferred size larger (see, e.g., Simpson et al. 2015). Taken together, these effects could contribute to the trend of increasing $r_s({\rm H}\alpha)/r_s(H_{F140W})$ with stellar mass. However, as described in Section 7.1, there are a number of other observational effects that work in the opposite direction, decreasing the $r_s({\rm H}\alpha)/r_s(H_{F140W})$ at high masses. Dust will

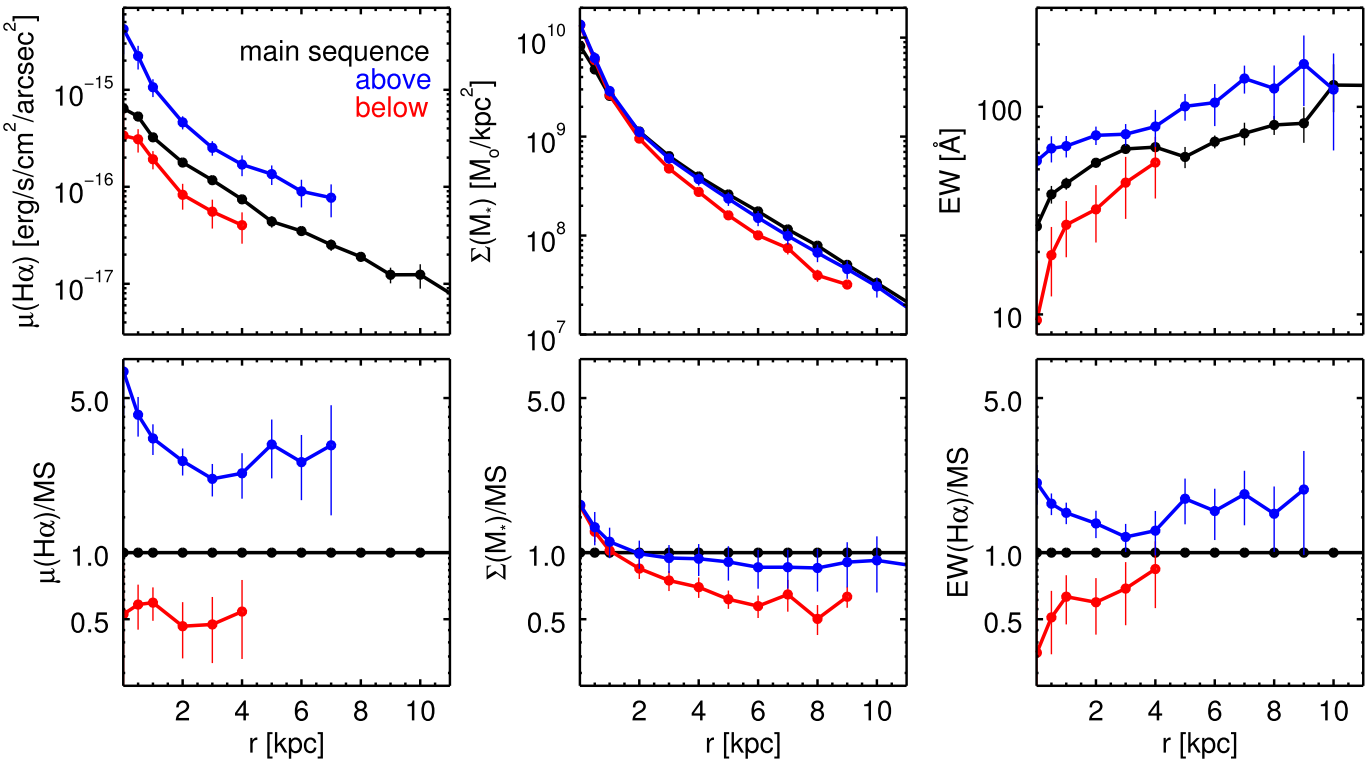

Figure 15. Top row: radial profiles of Hα, M_*, and EW(Hα) for galaxies with $M = 10^{10.5}$–$10^{11}\,M_\odot$. As previously, the colors delineate position with respect to the star-forming "MS": above (blue), on (black), and below (red). The bottom row shows these profiles normalized by the MS (with the black line divided out). Above the MS, the Hα (and EW(Hα)) is enhanced at all radii, but somewhat more so at small and large radii. Below the MS, the Hα (and EW(Hα)) is suppressed at all radii, but somewhat more so at small and large radii. There appears to be excess central stellar mass similarly above and below the MS.

also obscure the stellar continuum emission, meaning that the stellar mass could also be more concentrated than observed. Age gradients will also change the M/L, again adding more stellar mass at the center. Szomoru et al. (2013) estimate that galaxies are ∼25% more compact in mass than in light. AGNs contributing line emission to the Hα profiles will also work to decrease this ratio by adding extra flux and decreasing the size of the star formation. In sum, it seems more likely that observational effects will increase the $r_s(\mathrm{H}\alpha)/r_s(H_{F140W})$ with mass (and generally) than decrease it, but as the effects act in both directions, we cannot say with certainty which are more important.

While many observational effects could contribute to the mass dependence of the size ratio, this effect may also have a physical explanation. More massive galaxies have older mean ages. This means that a larger fraction of their star formation took place at earlier cosmic times. Hence, it is perhaps then reasonable that their stellar mass—the integral of their past star formation history—would be more compact than the gas disks with ongoing star formation. On the other hand, low-mass galaxies have younger mean ages, which means that their mass-weighted sizes are closer to the sizes of their star-forming disks.

7.4. Above and below the Main Sequence

One of the primary new observational results presented in this study is the first systematic description of where star formation occurs in galaxies above and below the star-forming sequence. That is, we describe the radial distribution of star formation in galaxies with relatively high and relatively low SFRs for their stellar mass. Previously, Whitaker et al. (2012) showed that the SEDs of galaxies above and below the MS are different from those on it. Above the MS, the SEDs are dusty but blue, which they interpreted as indicative of AGNs or merger-induced starbursts. Below the MS, the SEDs are not dusty but red, which they interpreted as indicative of star formation being shut down. Additionally, Wuyts et al. (2011b) showed that galaxies above and below the MS were structurally more compact and centrally concentrated than galaxies on the star-forming MS.

Hints as to what physical processes are driving a galaxy above or below the MS are given by these trends in stellar structure and SED shape. The next key piece of information is *where* the star formation is enhanced above and suppressed below the star-forming sequence, which we show here. For instance, if the primary physical processes driving galaxies above the MS are AGNs, central starbursts, or "compaction," we would expect Hα to be enhanced in the center but not at larger radii. If galaxies undergo "inside-out" quenching (e.g., Genzel et al. 2014a, Tacchella et al. 2016), we would expect galaxies below the MS to have Hα primarily suppressed in the center.

We find that star formation is spatially coherent. That is, star formation as traced by Hα is enhanced and depressed at all radii above and below the MS, respectively. Extra star formation is added at all radii above the MS and subtracted at all radii below it. We see no evidence for a preferred radial pattern with which star formation is boosted or suppressed. This does not happen in a particular part of galaxies. Whatever is responsible for boosting and suppressing star formation appears to be a global phenomenon, not limited to bulges or disks. This perhaps makes more sense in the context of scatter driven by variations in gas accretion rate rather than some

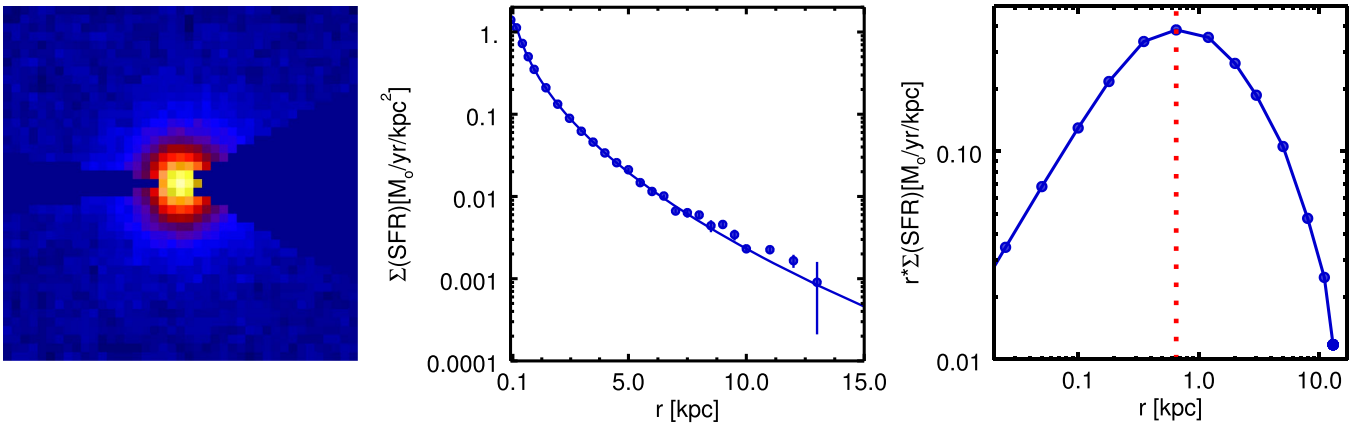

Figure 16. Stack of all Hα for the redshift epoch $0.7 < z < 1.5$ and the corresponding average radial distribution (left and middle). The right panel shows the probability distribution of star formation as a function of radius. This distribution is shown with a logarithmic x-axis and resampled for clarity. The peak of the probability distribution shows where the average star formed during this epoch: ~0.75 kpc from the center of it is home galaxy.

ubiquitous physical process. In other words, the similarity of the radial profiles appears consistent with a simple model in which the overall SFR scales with the gas accretion rate (averaged over some timescale) and the gas distributes itself in similar structures regardless of its accretion rate. However, truly understanding the physical underpinnings of the spatial coherence of star formation and the role of feedback will require the interpretive power of simulations.

Additionally, the spatially coherent Hα emission has a few specific implications, which we outline below. First, our results constrain the importance of AGN emission above the MS. One possibility is that galaxies above the star-forming MS are there because the bright UV+IR emission of an AGN was incorrectly interpreted as star formation. In this case, the Hα emission would be elevated in the center but the same as on the MS throughout the rest of the disk. This, however, is not what we observe: the Hα in the disk from 2 to 6 kpc is elevated, meaning that galaxies are not only above the MS due to misinterpreted AGNs.

Second, we characterize galaxies with respect to the star formation MS using their total SFRs (SFR(IR+UV)), which reflect the total obscured+unobscured ionizing flux from young stars. We then measure the distribution of Hα emission and see that it is elevated at all radii above the MS. Because Hα is an independent indicator of star formation, the fact that it is enhanced at all radii confirms that the scatter in the MS is real and due to variations in the SFR at fixed mass. If the observed MS scatter were due exclusively to measurement errors in the UV+IR SFRs, the Hα should not be enhanced or depressed in concert, but it is.

Third, the profiles provide information on the importance of mergers and galaxy encounters "pushing" galaxies above the MS. It is well established that interaction-driven gravitational torques can funnel gas to the center of a galaxy, inducing a burst of star formation (e.g., Hernquist 1989; Barnes & Hernquist 1991, 1996; Mihos & Hernquist 1996). In idealized merger simulations, Moreno et al. (2015) show that while star formation is enhanced in the central kiloparsec of interacting galaxies, it is *suppressed* everywhere else. Assuming that the results of Moreno et al. (2015) are correct, our results suggest that major mergers are not the *only* physical process driving the elevated star formation in galaxies above the star-forming MS. We observe that above the MS Hα is enhanced at all radii. It is not enhanced in the central kiloparsec and suppressed at larger galactocentric radii, as one would expect if star formation were mostly enhanced due to mergers. This suggests that some other processes in addition to major mergers are important for enhancing star formation in galaxies.

We note that some ambiguity is inherent in the interpretation of an average distribution of Hα because the distribution of Hα in individual galaxies could vary significantly from the average. Additionally, our stacking method cannot distinguish between local enhancements at random locations in the disk and global enhancement of the disks of individual galaxies.

Below the MS, many of the proposed mechanisms for suppressing star formation originate from the centers of galaxies, where AGNs live, bulges grow, and timescales are short. However, below the MS, what we observe is that star formation is suppressed throughout the disk, not just the center. This suggests that whatever mechanism we want to invoke for suppressing star formation must also be able to act at large radii.

Regardless of the physical reasons, across the SFR–M_* plane two important features are consistent: (1) the observed Hα distribution is always centrally peaked, and (2) the observed EW(Hα) is never centrally peaked. It will be interesting to compare the observed gas distributions directly to those in galaxy formation models.

7.5. Bulge Growth and Quenching at High Masses?

While Hα is enhanced at all radii in galaxies above the MS and suppressed at all radii below the MS, in the high-mass bin ($M = 10^{10.5}$–$10^{11}\,M_\odot$), the trends appear to have some radial dependence as well. To examine trends at high masses in more detail, in Figure 15 we show the same radial profiles of Hα, $H_{\rm F140W}$, and EW(Hα) above, on, and below the MS as in Figures 9 and 14. Here we also normalize by the MS profiles to highlight differences.

Above the MS, there is a central excess in Hα emission (left panels of Figure 15). The most straightforward interpretation of this central Hα excess is that we are witnessing star formation building bulges. Further, above the MS the EW(Hα) is elevated both at the center and beyond $r > 4$ kpc relative to galaxies on the MS. Interpreting the EW(Hα) as sSFR, above the MS, star formation is increasing the curvature or the stellar mass surface density profile more than it does on the MS. As the curvature of the surface brightness profile is correlated with the

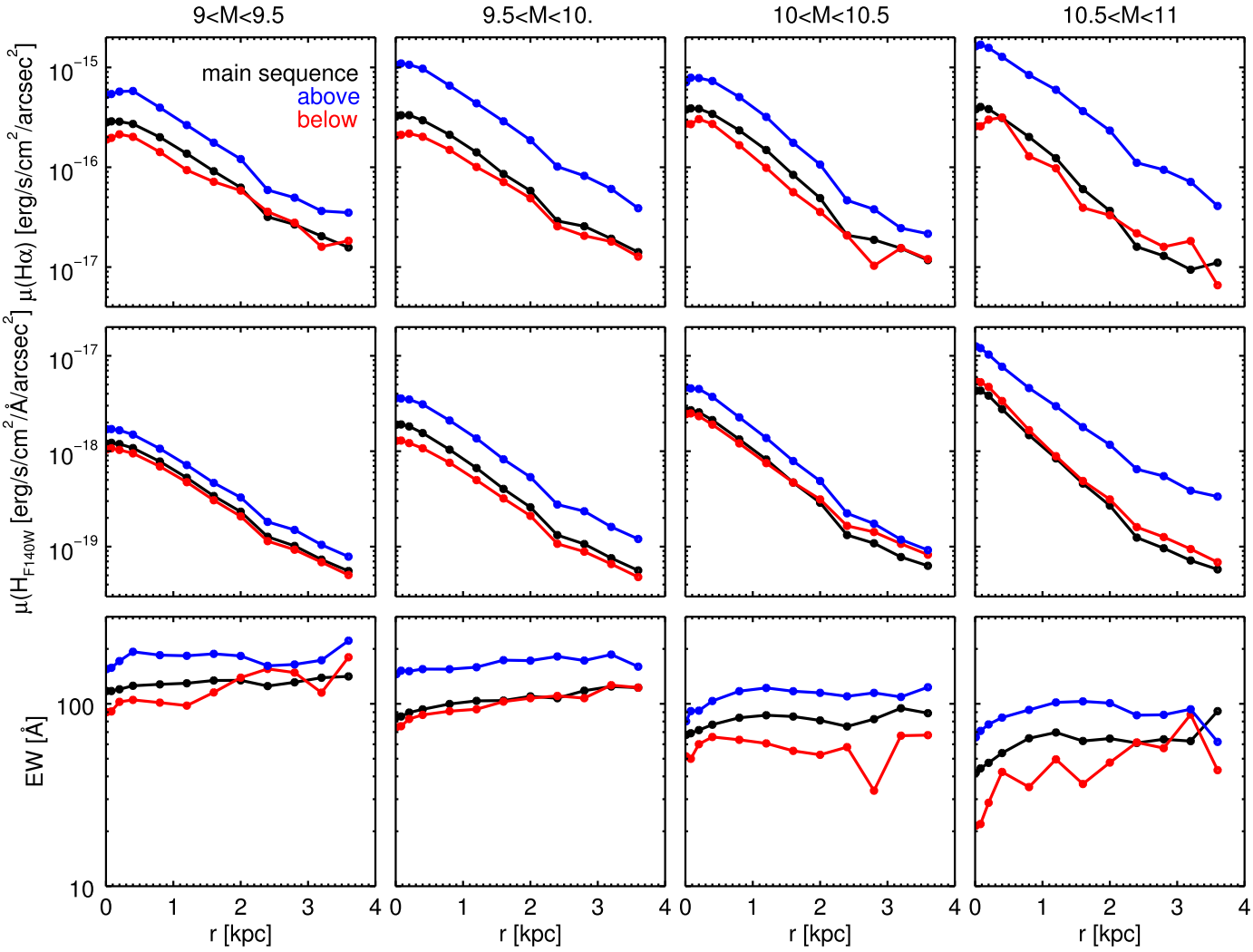

Figure 17. Average deprojected, r_e-normalized radial profiles of Hα, $H_{\rm F140W}$, and EW(Hα) as a function of mass.

bulge-to-disk ratio (Simmons & Urry 2008), this corroborates the notion that star formation is building bulges above the MS at $M = 10^{10.5}$–$10^{11}\,M_{\odot}$.

While the most straightforward interpretation of the excess central Hα emission is that it is due to star formation building bulges, it could also be due to AGNs. As mentioned in Section 2.3, galaxies with X-ray luminosity $L_x > 10^{42.5}$ erg s^{-1} or a very obvious broad-line component are excluded from the analysis in this paper. So the excess central Hα emission exists when galaxies hosting obvious AGNs are excluded. However, with an extremely conservative cut on broad-line AGNs in which galaxies with even marginal elongation in the spectral direction are excluded, the central excess in Hα is significantly less. Hence, we cannot rule out that this central Hα enhancement is driven by emission from AGNs. If this turns out to be the case, it would mean that supermassive black holes are growing in this region of parameter space. We note that because the IR/Hα in this bin is so high, it is likely that there is significant dust attenuation. As shown in Nelson et al. (2016), this will particularly impact the centers of galaxies. This means that the excess in central ionizing flux from star formation, AGNs, or (likely) both would actually be even larger if it were not attenuated.

Regardless of whether the excess central Hα emission is due to star formation or AGNs, it indicates that gas is being driven to the center of these massive galaxies above the MS. Thus, this observational signature could conceivably support the following theoretical picture for the evolution of gas-rich disks. If the high SFRs in galaxies above the MS are fueled by elevated gas accretion rates, the disks of these galaxies are likely to be gas-rich. In these gas-rich environments, it has been suggested that gravitational torques induced by violent disk instability could drive gas rapidly inward by viscous and dynamical friction (Noguchi 1999; Dekel et al. 2009b, 2013; Krumholz & Burkert 2010; Bournaud et al. 2011; Genzel et al. 2011; Cacciato et al. 2012; Elmegreen et al. 2012; Forbes et al. 2012, 2014). Once in the center, this gas could fuel the bulge and/or black hole growth evidenced by the excess central Hα emission.

Below the MS, there is a strong central dip in the radial EW(Hα) profile (Figure 15, right). Interpreting the EW(Hα) as sSFR, this means that the growth of galaxies below the MS is centrally suppressed. The stellar mass doubling time in the centers of these galaxies is significantly lower than at larger radii. During the epoch $0.7 < z < 1.5$, in this mass range ($M = 10^{10.5}$–$10^{11}\,M_{\odot}$) the quenched fraction roughly doubles (from ~30% to 60%). Since the SFRs of galaxies must fall

below the MS on their way to quenchdom, mapping where star formation is suppressed in this region of parameter space is the most direct observational indicator of how galaxies quench. As such, the centrally depressed EW(Hα) could be taken as evidence that galaxies quench from the inside out (Genzel et al. 2014a; Tacchella et al. 2015a). Here we show this for the first time explicitly below the MS, where it is most straightforward to interpret in the context of star formation quenching.

Similarly above and below the MS, we find high central stellar mass surface densities. As inferred from the $H_{\rm F140W}$ emission, the stellar mass surface density in the central kiloparsec of these massive galaxies is similar above and below the MS. In both, it is higher than in galaxies on the MS. This result is qualitatively consistent with measurements of Sérsic indices by Wuyts et al. (2011b), but this is the first direct measurement of the average surface brightness profiles of galaxies above and below the MS.

The structural similarity between galaxies above and below the MS could indicate an evolutionary link between them. If this is the case, then the distribution of Hα in galaxies above the MS evolves into the distribution of Hα emission in galaxies below the MS, and perhaps there is even a causal link between them. Above the MS, we observe a central enhancement in Hα emission that could be interpreted as star formation building bulges or AGN activity indicative of growing black holes. Below the MS, we observe a central depression in EW(Hα), suggesting a suppression of central star formation. Taken together, these observational signatures could be viewed in the context of an evolutionary pathway from bulge or supermassive black hole growth to quenching (e.g., Wuyts et al. 2011b; Genzel et al. 2014a; Lang et al. 2014; Tacchella et al. 2015a). Whatever process we observe under way above the MS, there are theoretical indications that it is capable of suppressing star formation, causing galaxies to fall below the MS. Above the MS, AGNs can in principle drive gas out of the centers of their host galaxies, efficiently removing the fuel for star formation (see, e.g., Croton et al. 2006). Large bulges are also in principle capable of stabilizing galaxy disks and suppressing star formation from the inside out ("gravitational quenching"; Martig et al. 2009; Genzel et al. 2014a). Observationally, it seems that regardless of the physical cause, galaxies quench after reaching a central stellar surface density threshold (e.g., Kauffmann et al. 2003, Franx et al. 2008; Bell et al. 2012; Cheung et al. 2012, Wake et al. 2012, Fang et al. 2013; Lang et al. 2014; van Dokkum et al. 2014; Barro et al. 2015).

However, we do note one caveat regarding this bulge growth to inside-out quenching picture. First, even in massive galaxies below the MS, in an absolute sense, our observed Hα is centrally peaked. On average, there is not a hole in the observed Hα emission in these galaxies. That is, although the Hα is centrally depressed in two relative senses (relative to the $H_{\rm F140W}$ and relative to the MS Hα), in an absolute sense, the Hα is *not* centrally depressed. If we interpret this observed Hα emission as star formation, it means that although we are seeing less star formation relative to the stellar mass in the centers of these galaxies, the central star formation has by no means shut off. So while we may be seeing some suppression of star formation in the center of these galaxies below the MS, it is not "quenching" in the sense of a complete cessation of star formation. This appears to contradict recent results finding Hα rings to be common among massive galaxies (Genzel et al. 2014a). However, this could be due to the fact that, lacking kinematic information, we cannot correct for the central Hα emission added by shocks from winds and AGNs (Förster Schreiber et al. 2014; Genzel et al. 2014b). This effect could explain the discrepancy if these galaxies below the MS have high central star formation surface densities or AGN driving winds. Additionally, our averaged profiles do not exclude the possibility that some individual galaxies have rings at $z \sim 1$, which are offset by galaxies with excess emission in the center. Finally, not all galaxies that we observe below the MS will necessarily quench; some may simply have temporarily lower SFRs due, for instance, to a period of lower gas accretion rates. These galaxies, which could just have somewhat suppressed star formation throughout their disks, could dilute an inside-out quenching signature.

7.6. The Average Spatial Distribution of Star Formation from $z = 0.7$ to 1.5

In Sections 4 and 5 we determined the radial profiles of star formation as a function of M_* and SFR. Here we briefly analyze the radial distribution of all star formation at this epoch, that is, at what distance from the center of a galaxy is a star most likely to form. The average Hα image of all selected galaxies is shown in Figure 16. This is the average spatial distribution of Hα in galaxies with $10^9\,M_\odot < M_* < 10^{11}\,M_\odot$ during the epoch $0.7 < z < 1.5$. Each galaxy has an Hα map with a depth of two orbits on *HST*. We summed the Hα maps of 3200 galaxies, creating the equivalent of a 5400-orbit Hα image. This average Hα image is the deepest Hα image in existence for galaxies at this epoch. With this stacked 5352-orbit *HST* image, we can trace the radial distribution of Hα down to a surface brightness limit of $1 \times 10^{-18}\,{\rm erg\,s^{-1}\,cm^{-2}\,arcsec^{-2}}$. This allows us to map the distribution of Hα emission out to ∼14 kpc, where the star formation surface density is $4 \times 10^{-4}\,M_\odot\,{\rm yr^{-1}\,kpc^{-2}}$ (Kennicutt 1998).

In Figure 16 we show the probability distribution of star formation as a function of radius for galaxies at this epoch. We compute the probability distribution by normalizing the star formation surface density in each annulus by the area of that annulus. As we did not normalize by the $H_{\rm F140W}$ flux here, the peak of this distribution reflects the most likely place for a random H II region within a galaxy to exist for galaxies in this mass and redshift range. The probability distribution of Hα as a function of radius has a peak at 0.75 kpc, which is inside a resolution element. However, data of higher spatial resolution are needed to actually resolve this peak. If we assume that Hα is a good tracer of star formation and this takes place mostly in star-forming galaxies with $10^9\,M_\odot < M_* < 10^{11}\,M_\odot$, then the peak of the probability distribution yields information about where star formation is most likely to occur within a galaxy. This means that during the epoch $0.7 < z < 1.5$, when ∼33% of the total star formation in the history of the universe occurred, the most likely place for a new star to be born was within ∼1 kpc or the center of its home galaxy.

8. CONCLUSIONS

In this paper, we studied galaxy growth through star formation during the epoch $0.7 < z < 1.5$ through a new window provided by the WFC3 G141 grism on *HST*. This slitless grism spectroscopy from space, with its combination of high spatial resolution and low spectral resolution, yields resolved information on how the Hα emission is distributed

within galaxies. We have this information for an Hα and $H_{\rm F140W}$ flux-limited sample of 3200 star-forming galaxies over a large swath of the SFR–M_* plane from 10^9 to $10^{11}\,M_\odot$. Hα can be used as a proxy for star formation, although dust is a significant uncertainty (Section 7.1). The most important new observational result of our study is the behavior of the Hα profiles above and below the MS: remarkably, star formation is enhanced at all radii above the MS and suppressed at all radii below the MS (Figure 14). This means that the scatter in the star-forming sequence is real. It also suggests that the primary mode of star formation is similar across all regions of this parameter space.

Across the expanse of the SFR–M_* plane, the radial distribution of star formation as traced by Hα can be characterized in the following way. Most of the Hα emission lies in galactic disks (Figure 5), which are well aligned with the stellar distribution (Figure 12). To first order, Hα emission and stellar continuum emission trace each other quite well. On average, the Hα surface density is always highest in the centers of galaxies, just like the stellar mass surface density. On the other hand, the EW(Hα) and the inferred sSFR are, on average, *never* highest in the centers of galaxies (Figure 9). Taken at face value, this means that star formation is slightly more extended than the existing stars (Figure 6), demonstrating that galaxies at this epoch are growing in size due to star formation.

Taking the observed parameters at face value is justified for galaxies with $M_* < 10^{10}\,M_\odot$ that have little dust attenuation (Nelson et al. 2016). Thus, in these galaxies, most star formation occurs in disks, and these disks of star formation are more spatially extended than the disks of stars. Galaxies with $M_* > 10^{10}\,M_\odot$, on the other hand, have significant dust attenuation. In these galaxies Hα cannot be interpreted directly as star formation and $H_{\rm F140W}$ cannot be interpreted directly as stellar mass. Nelson et al. (2016) showed that there is significant dust attenuation toward the star formation at the centers of these galaxies. Thus, while most of the Hα emission lies in exponential disks, dust-obscured star formation is building bulges as well. Deriving dust-corrected radial profiles of star formation above and below the MS is a crucial next step. Confirming that the star formation is truly more extended than the stellar mass in these galaxies requires a measurement of the dust attenuation toward their stars.

The results in this study can be extended in many ways. In principle, the same data set can be used to study the spatial distribution of [O III] emission at higher redshifts, although it is more difficult to interpret and the fact that it is a doublet poses practical difficulties. With submillimeter interferometers such as NOEMA and ALMA the molecular gas reservoir can be mapped. Although it will be difficult to match the resolution and sample size that we reach in this study, this combination of data is crucial to understand the physical drivers of star formation and quenching. Finally, joint studies of the evolution of the distribution of star formation and the stellar mass can provide constraints on the importance of mergers and stellar migration in the buildup of present-day disks.

We thank the referee for their thoughtful report, which improved the paper. This work is based on observations taken by the 3D-*HST* Treasury Program (GO 12177 and 12328) with the NASA/ESA *HST*, which is operated by the Associations of Universities for Research in Astronomy, Inc., under NASA contract NAS5-26555. E.J.N. gratefully acknowledges support from the National Science Foundation Graduate Research Fellowship.

APPENDIX

In this paper we investigate the average radial distribution of Hα emission by stacking the Hα maps of individual galaxies and computing the flux in circular apertures on this stack. With this methodology, we average over the distribution of inclination angles, position angles, and sizes of galaxies that go into each stack. The simplicity of this method has a number of advantages. First, it requires no assumptions about the intrinsic properties of galaxies. Second, it allows us to measure the average size of the Hα distribution in the star-forming disk. Finally, because the image plane is left intact, we can correct for the PSF.

To complement this analysis, here we present the average deprojected, radially normalized distribution of Hα. We do this to test the effect of projection and a heterogenous mix of sizes on the shape of the radial profile of Hα, to ensure that trends were not washed out with the simpler methodology employed in the rest of the paper.

To do this, we use GALFIT (Peng et al. 2002) to derive the effective radius, axis ratio, and position angle of each galaxy from its $H_{\rm F140W}$ stellar continuum image. We adopt effective radii and axis ratios from van der Wel et al. (2014b) and measure position angles from the interlaced postage stamps using a similar methodology. We correct for the inclination angle of each galaxy by deprojecting the (x, y) pixel grid of its image based on the inclination angle implied by the axis ratio. The surface brightness profile is computed by measuring the flux in deprojected radial apertures. In practice, this is done simply by extracting the radial profile of each galaxy in elliptical apertures defined by the position angle, axis ratio, and center of the $H_{\rm F140W}$ image. The extraction apertures were normalized by the $H_{\rm F140W}$ effective radius of each galaxy. A radial profile in deprojected, r_e-normalized space is derived for each galaxy. These individual galaxy profiles are flux-normalized by their integrated $H_{\rm F140W}$ magnitude and summed to derive the mean radial distribution.

The average deprojected, r_e-normalized radial profiles of Hα, $H_{\rm F140W}$, and EW(Hα) are shown in Figure 17. In general, the qualitative trends seen here are the same as those described in the main text. For the region $0.5 < r_e < 3$ the radial profile of Hα remains consistent with an exponential at all masses, above, on, and below the star-forming sequence. The radial profiles of both Hα and $H_{\rm F140W}$ are somewhat less centrally peaked than the analogous profiles in Figure 9. This is expected of disk-dominated galaxies under different orientation angles as flux from the disks of edge-on galaxies could be projected onto the center. Additionally, stacking galaxies of different sizes can result in a somewhat steeper (higher-n) profile than the individual galaxies that went into it (see van Dokkum et al. 2010). Because the shapes of the Hα and $H_{\rm F140W}$ profiles are similarly affected by deriving the profiles with this different methodology, the shape of the EW(Hα) profiles remains largely unchanged.

REFERENCES

Abramson, L. E., Kelson, D. D., Dressler, A., et al. 2014, ApJL, 785, L36
Adelberger, K. L., & Steidel, C. C. 2000, ApJ, 544, 218
Agertz, O., Teyssier, R., & Moore, B. 2011, MNRAS, 410, L1391

Atek, H., Malkan, M., McCarthy, P., et al. 2010, ApJ, 723, 104
Aumer, M., White, S. D. M., Naab, T., & Scannapieco, C. 2013, MNRAS, 434, 3142
Barnes, J. E., & Hernquist, L. 1996, ApJ, 471, 115
Barnes, J. E., & Hernquist, L. E. 1991, ApJL, 370, L65
Barro, G., Faber, S. M., Koo, D. C., et al. 2015, ApJ, submitted (arXiv:109:00469)
Behroozi, P. S., Marchesini, D., Wechsler, R. H., et al. 2013, ApJL, 777, L10
Bell, E. F., & de Jong, R. 2001, ApJ, 550, 212
Bell, E. F., Papovich, C., Wolf, C., et al. 2005, ApJ, 625, 23
Bell, E. F., van der Wel, A., Papovich, C., et al. 2012, ApJ, 753, 167
Boada, S., Tilvi, V., Papovich, C., et al. 2015, ApJ, 803, 104
Bournaud, F., Dekel, A., Teyssier, R., et al. 2011, ApJL, 741, L33
Brammer, G., Pirzkal, N., McCullough, P., & MacKenty, J. 2014, Time-varying Excess Earth-glow Backgrounds in the WFC3/IR Channel Tech. Rep
Brammer, G. B., Sánchez-Janssen, R., Labbé, I., et al. 2012a, ApJL, 758, L17
Brammer, G. B., van Dokkum, P. G., & Coppi, P. 2008, ApJ, 686, 1503
Brammer, G. B., van Dokkum, P. G., Franx, M., et al. 2012b, ApJS, 200, 13
Brammer, G. B., van Dokkum, P. G., Illingworth, G. D., et al. 2013, ApJL, 765, L2
Brennan, R., Pandya, V., Somerville, R. S., et al. 2015, MNRAS, submitted (arXiv:1501.06840)
Brinchmann, J., Charlot, S., White, S. D. M., et al. 2004, MNRAS, 351, 1151
Brooks, A. M., Governato, F., Quinn, T., Brook, C. B., & Wadsley, J. 2009, ApJ, 694, 396
Brooks, A. M., Solomon, A. R., Governato, F., et al. 2011, ApJ, 728, 51
Bruce, V. A., Dunlop, J. S., McLure, R. J., et al. 2014, MNRAS, 444, L1660
Bruzual, G., & Charlot, S. 2003, MNRAS, 344, 1000
Buitrago, F., Conselice, C. J., Epinat, B., et al. 2014, MNRAS, 439, 1494
Buitrago, F., Trujillo, I., Conselice, C. J., et al. 2008, ApJL, 687, L61
Buitrago, F., Trujillo, I., Conselice, C. J., et al. 2013, MNRAS, 428, 1460
Cacciato, M., Dekel, A., & Genel, S. 2012, MNRAS, 421, 818
Calzetti, D., Armus, L., Bohlin, R. C., et al. 2000, ApJ, 533, 682
Calzetti, D., Kinney, A. L., & Storchi-Bergmann, T. 1994, ApJ, 429, 582
Chabrier, G. 2003, PASP, 115, 763
Charlot, S., & Fall, S. M. 2000, ApJ, 539, 718
Cheung, E., Faber, S. M., Koo, D. C., et al. 2012, ApJ, 760, 131
Contini, T., Garilli, B., Le Fèvre, O., et al. 2012, A&A, 539, A91
Croton, D. J., Springel, V., White, S. D. M., et al. 2006, MNRAS, 365, 11
Daddi, E., Dickinson, M., Morrison, G., et al. 2007, ApJ, 670, 156
Dalcanton, J. J., Spergel, D. N., & Summers, F. J. 1997, ApJ, 482, 659
Dale, D. A., & Helou, G. 2002, ApJ, 576, 159
Damen, M., Labbé, I., Franx, M., et al. 2009, ApJ, 690, 937
Dekel, A., & Birnboim, Y. 2006, MNRAS, 368, L2
Dekel, A., Birnboim, Y., Engel, G., et al. 2009a, Natur, 457, 451
Dekel, A., Sari, R., & Ceverino, D. 2009b, ApJ, 703, 785
Dekel, A., Zolotov, A., Tweed, D., et al. 2013, MNRAS, 435, 999
Domínguez, A., Siana, B., Henry, A. L., et al. 2013, ApJ, 763, 145
Dutton, A. A., & van den Bosch, F. C. 2012, MNRAS, 421, 608
Elbaz, D., Daddi, E., Le Borgne, D., et al. 2007, A&A, 468, 33
Elmegreen, B. G., & Elmegreen, D. M. 2005, ApJ, 627, 632
Elmegreen, B. G., Elmegreen, D. M., Fernandez, M. X., & Lemonias, J. J. 2009, ApJ, 692, 12
Elmegreen, B. G., Zhang, H.-X., & Hunter, D. A. 2012, ApJ, 747, 105
Epinat, B., Contini, T., Le Fèvre, O., et al. 2009, A&A, 504, 789
Epinat, B., Tasca, L., Amram, P., et al. 2012, A&A, 539, A92
Erb, D. K., Steidel, C. C., Shapley, A. E., et al. 2006a, ApJ, 646, 107
Erb, D. K., Steidel, C. C., Shapley, A. E., et al. 2006b, ApJ, 647, 128
Fall, S. M., & Efstathiou, G. 1980, MNRAS, 193, 189
Fang, J. J., Faber, S. M., Koo, D. C., & Dekel, A. 2013, ApJ, 776, 63
Ferguson, H. C., Dickinson, M., Giavalisco, M., et al. 2004, ApJL, 600, L107
Ferreras, I., Pasquali, A., Khochfar, S., et al. 2012, AJ, 144, 47
Forbes, J., Krumholz, M., & Burkert, A. 2012, ApJ, 754, 48
Forbes, J. C., Krumholz, M. R., Burkert, A., & Dekel, A. 2014, MNRAS, 438, 1552
Förster Schreiber, N. M., Genzel, R., Bouché, N., et al. 2009, ApJ, 706, 1364
Förster Schreiber, N. M., Genzel, R., Lehnert, M. D., et al. 2006, ApJ, 645, 1062
Förster Schreiber, N. M., Genzel, R., Newman, S. F., et al. 2014, ApJ, 787, 38
Förster Schreiber, N. M., Shapley, A. E., Erb, D. K., et al. 2011a, ApJ, 731, 65
Förster Schreiber, N. M., Shapley, A. E., Genzel, R., et al. 2011b, ApJ, 739, 45
Franx, M., van Dokkum, P. G., Schreiber, N. M. F., et al. 2008, ApJ, 688, 770
Fumagalli, M., Patel, S. G., Franx, M., et al. 2013, in IAU Symp.295, The Intriguing Life of Massive Galaxies, ed. D. Thomas, A. Pasquali, & I. Ferreras (Cambridge: Cambridge Univ. Press), 9
Geach, J. E., Smail, I., Best, P. N., et al. 2008, MNRAS, 388, 1473
Genel, S., Fall, S. M., Hernquist, L., et al. 2015, ApJL, 804, L40
Genzel, R., Burkert, A., Bouché, N., et al. 2008, ApJ, 687, 59
Genzel, R., Förster Schreiber, N. M., Lang, P., et al. 2014a, ApJ, 785, 75
Genzel, R., Förster Schreiber, N. M., Rosario, D., et al. 2014b, ApJ, 796, 7
Genzel, R., Newman, S., Jones, T., et al. 2011, ApJ, 733, 101
Giavalisco, M., Steidel, C. C., & Macchetto, F. D. 1996, ApJ, 470, 189
González, V., Labbé, I., Bouwens, R. J., et al. 2010, ApJ, 713, 115
Governato, F., Brook, C., Mayer, L., et al. 2010, Natur, 463, 203
Grogin, N. A., Kocevski, D. D., Faber, S. M., et al. 2011, ApJS, 197, 35
Guedes, J., Callegari, S., Madau, P., & Mayer, L. 2011, ApJ, 742, 76
Guo, Y., Giavalisco, M., Ferguson, H. C., et al. 2012, ApJ, 757, 120
Hayward, C. C., Lanz, L., Ashby, M. L. N., et al. 2014, MNRAS, 445, 1598
Hernquist, L. 1989, Natur, 340, 687
Hopkins, A. M., Connolly, A. J., Haarsma, D. B., & Cram, L. E. 2001, AJ, 122, 288
Huang, S., Haynes, M. P., Giovanelli, R., & Brinchmann, J. 2012, ApJ, 756, 113
Hummels, C. B., & Bryan, G. L. 2012, ApJ, 749, 140
Jones, T., Ellis, R. S., Richard, J., & Jullo, E. 2013, ApJ, 765, 48
Jones, T., Wang, X., Schmidt, K. B., et al. 2015, AJ, 149, 107
Karim, A., Schinnerer, E., Martínez-Sansigre, A., et al. 2011, ApJ, 730, 61
Kashino, D., Silverman, J. D., Rodighiero, G., et al. 2013, ApJL, 777, L8
Kauffmann, G., Heckman, T., White, S., et al. 2003, MNRAS, 341, 54
Kennicutt, R. C., Jr. 1998, ApJ, 498, 541
Keres, D., Katz, N., Fardal, M., Davé, R., & Weinberg, D. H. 2009, MNRAS, 395, L160
Keres, D., Katz, N., Weinberg, D. H., & Davé, R. 2005, MNRAS, 363, L2
Koekemoer, A. M., Faber, S. M., Ferguson, H. C., et al. 2011, ApJS, 197, 36
Kornei, K. A., Shapley, A. E., Martin, C. L., et al. 2012, ApJ, 758, 135
Kriek, M., Shapley, A. E., Reddy, N. A., & Siana, B. 2015, ApJS, 218, 15
Kriek, M., van Dokkum, P. G., Franx, M., Illingworth, G. D., & Magee, D. K. 2009, ApJL, 705, L71
Krist, J. 1995, in ASP Conf. Ser. 77, Astronomical Data Analysis Software and Systems IV, ed. R. A. Shaw, H. E. Payne, & J. J. E. Hayes (San Francisco, CA: ASP), 349
Krumholz, M., & Burkert, A. 2010, ApJ, 724, 895
La Barbera, F., Ferreras, I., de Carvalho, R. R., et al. 2012, MNRAS, 426, 2300
Labbe, I., Huang, J., Franx, M., et al. 2005, ApJL, 624, L81
Lang, P., Wuyts, S., Somerville, R. S., et al. 2014, ApJ, 788, 11
Leja, J., van Dokkum, P. G., Franx, M., & Whitaker, K. E. 2015, ApJ, 798, 115
Leja, J., van Dokkum, P. G., Momcheva, I., et al. 2013, ApJL, 778, L24
Lu, Z., Mo, H. J., Lu, Y., et al. 2014, MNRAS, 439, 1294
Magdis, G. E., Rigopoulou, D., Huang, J.-S., & Fazio, G. G. 2010, MNRAS, 401, 1521
Maiolino, R., Nagao, T., Grazian, A., et al. 2008, A&A, 488, 463
Mancini, C., Förster Schreiber, N. M., Renzini, A., et al. 2011, ApJ, 743, 86
Marinacci, F., Pakmor, R., & Springel, V. 2013, MNRAS, 437, 1750
Marsan, Z. C., Marchesini, D., Brammer, G. B., et al. 2015, ApJ, 801, 133
Martig, M., Bournaud, F., Teyssier, R., & Dekel, A. 2009, ApJ, 707, 250
Mihos, J. C., & Hernquist, L. 1996, ApJ, 464, 641
Minchev, I., Martig, M., Streich, D., et al. 2015, ApJ, 804, 9
Mitchell, P. D., Lacey, C. G., Baugh, C. M., & Cole, S. 2013, MNRAS, 435, 87
Mo, H. J., Mao, S., & White, S. D. M. 1998, MNRAS, 295, 319
Momcheva, I. G., Brammer, G. B., van Dokkum, P. G., et al. 2016, ApJS, 225, 27
Momcheva, I. G., Lee, J. C., Ly, C., et al. 2013, AJ, 145, 47
Moreno, J., Torrey, P., Ellison, S. L., et al. 2015, MNRAS, 448, 1107
Mosleh, M., Williams, R. J., Franx, M., et al. 2012, ApJL, 756, L12
Moster, B. P., Naab, T., & White, S. D. M. 2013, MNRAS, 428, 3121
Muzzin, A., van Dokkum, P., Kriek, M., et al. 2010, ApJ, 725, 742
Nelson, D., Genel, S., Vogelsberger, M., et al. 2015, MNRAS, 448, 59
Nelson, E., van Dokkum, P., Franx, M., et al. 2014, Natur, 513, 394
Nelson, E. J., van Dokkum, P. G., Brammer, G., et al. 2012, ApJL, 747, L28
Nelson, E. J., van Dokkum, P. G., Momcheva, I., et al. 2013, ApJL, 763, L16
Nelson, E. J., van Dokkum, P. G., Momcheva, I. G., et al. 2016, ApJL, 817, L9
Newman, S. F., Genzel, R., Förster-Schreiber, N. M., et al. 2012, ApJ, 761, 43
Noeske, K. G., Weiner, B. J., Faber, S. M., et al. 2007, ApJL, 660, L43
Noguchi, M. 1999, ApJ, 514, 77
Oesch, P. A., Bouwens, R. J., Carollo, C. M., et al. 2010, ApJL, 709, L21
Pannella, M., Carilli, C. L., Daddi, E., et al. 2009, ApJL, 698, L116
Papovich, C., Labbé, I., Quadri, R., et al. 2015, ApJ, 803, 26
Patel, S. G., van Dokkum, P. G., Franx, M., et al. 2013, ApJ, 766, 15
Peng, C. Y., Ho, L. C., Impey, C. D., & Rix, H.-W. 2002, AJ, 124, 266
Peth, M. A., Lotz, J. M., Freeman, P. E., et al. 2016, MNRAS, 458, 963

Price, S. H., Kriek, M., Brammer, G. B., et al. 2014, ApJ, 788, 86
Queyrel, J., Contini, T., Kissler-Patig, M., et al. 2012, A&A, 539, A93
Reddy, N. A., Erb, D. K., Pettini, M., Steidel, C. C., & Shapley, A. E. 2010, ApJ, 712, 1070
Reddy, N. A., Kriek, M., Shapley, A. E., et al. 2015, arXiv:1504.02782
Reddy, N. A., Steidel, C. C., Fadda, D., et al. 2006, ApJ, 644, 792
Rosario, D. J., Santini, P., Lutz, D., et al. 2013, ApJ, 771, 63
Roškar, R., Debattista, V. P., Stinson, G. S., et al. 2008, ApJL, 675, L65
Sales, L. V., Navarro, J. F., Schaye, J., et al. 2010, MNRAS, 409, 1541
Sales, L. V., Navarro, J. F., Theuns, T., et al. 2012, MNRAS, 423, 1544
Salim, S., Rich, R. M., Charlot, S., et al. 2007, ApJS, 173, 267
Sanders, R. L., Shapley, A. E., Kriek, M., et al. 2015, ApJ, 799, 138
Savaglio, S., Glazebrook, K., Le Borgne, D., et al. 2005, ApJ, 635, 260
Scannapieco, C., Wadepuhl, M., Parry, O. H., et al. 2012, MNRAS, 423, L1726
Sérsic, J. L. 1968, Atlas de Galaxias Australes (Cordoba: Observatorio Astronomico)
Shapiro, K. L., Genzel, R., Quataert, E., et al. 2009, ApJ, 701, 955
Shapley, A. E., Reddy, N. A., Kriek, M., et al. 2015, ApJ, 801, 88
Shapley, A. E., Steidel, C. C., Pettini, M., & Adelberger, K. L. 2003, ApJ, 588, 65
Shen, S., Mo, H. J., White, S. D. M., et al. 2003, MNRAS, 343, 978
Simmons, B. D., & Urry, C. M. 2008, ApJ, 683, 644
Simpson, J. M., Smail, I., Swinbank, A. M., et al. 2015, ApJ, 799, 81
Skelton, R. E., Whitaker, K. E., Momcheva, I. G., et al. 2014, ApJS, 214, 24
Sobral, D., Best, P. N., Geach, J. E., et al. 2009, MNRAS, 398, 75
Sobral, D., Best, P. N., Matsuda, Y., et al. 2012, MNRAS, 420, 1926
Sobral, D., Matthee, J., Best, P. N., et al. 2015, MNRAS, 451, 2303
Stinson, G. S., Bovy, J., Rix, H.-W., et al. 2013, MNRAS, 436, 625
Stott, J. P., Sobral, D., Swinbank, A. M., et al. 2014, MNRAS, 443, 2695
Swinbank, M., Smail, I., Sobral, D., et al. 2012, ApJ, 760, 130
Szomoru, D., Franx, M., van Dokkum, P. G., et al. 2010, ApJ, 714, 244
Szomoru, D., Franx, M., van Dokkum, P. G., et al. 2013, ApJ, 763, 73
Tacchella, S., Carollo, C. M., Renzini, A., et al. 2015a, Sci, 348, 314
Tacchella, S., Dekel, A., Carollo, C. M., et al. 2016, MNRAS, 458, 242
Tacchella, S., Lang, P., Carollo, C. M., et al. 2015b, ApJ, 802, 101
Toft, S., van Dokkum, P., Franx, M., et al. 2007, ApJ, 671, 285
Trujillo, I., Forster Schreiber, N. M., Rudnick, G., et al. 2006, ApJ, 650, 18
Übler, H., Naab, T., Oser, L., et al. 2014, MNRAS, 443, 2092
Utomo, D., Kriek, M., Labbé, I., et al. 2014, ApJ, 783, 30
van den Bosch, F. C. 2001, MNRAS, 327, 1334
van der Wel, A., Bell, E. F., Häussler, B., et al. 2012, ApJS, 203, 24
van der Wel, A., Chang, Y.-Y., Bell, E. F., et al. 2014a, ApJL, 792, L6
van der Wel, A., Franx, M., van Dokkum, P. G., et al. 2014b, ApJ, 788, 28
van Dokkum, P. G., Bezanson, R., van der Wel, A., et al. 2014, ApJ, 791, 45
van Dokkum, P. G., Brammer, G., Fumagalli, M., et al. 2011, ApJL, 743, L15
van Dokkum, P. G., Franx, M., Fabricant, D., Illingworth, G. D., & Kelson, D. D. 2000, ApJ, 541, 95
van Dokkum, P. G., Leja, J., Nelson, E. J., et al. 2013, ApJL, 771, L35
van Dokkum, P. G., Nelson, E. J., Franx, M., et al. 2015, ApJ, 813, 23
van Dokkum, P. G., Whitaker, K. E., Brammer, G., et al. 2010, ApJ, 709, 1018
Wang, B., & Heckman, T. M. 1996, ApJ, 457, 645
Wake, D., van Dokkum, P. G., & Franx, M. 2012, ApJL, 751, L44
Whitaker, K. E., Franx, M., Bezanson, R., et al. 2015, ApJ, 811, L12
Whitaker, K. E., Franx, M., Leja, J., et al. 2014, ApJ, 795, 104
Whitaker, K. E., Labbé, I., van Dokkum, P. G., et al. 2011, ApJ, 735, 86
Whitaker, K. E., van Dokkum, P. G., Brammer, G., & Franx, M. 2012, ApJL, 754, L29
White, S. D. M., & Rees, M. J. 1978, MNRAS, 183, L341
Williams, R. J., Quadri, R. F., Franx, M., et al. 2010, ApJ, 713, 738
Wisnioski, E., Förster Schreiber, N. M., Wuyts, S., et al. 2015, ApJ, 799, 209
Wuyts, E., Kurk, J., Förster Schreiber, N. M., et al. 2014, ApJL, 789, L40
Wuyts, E., Wisnioski, E., Fossati, M., et al. 2016, ApJ, 827, 74
Wuyts, S., Förster Schreiber, N. M., Genzel, R., et al. 2012, ApJ, 753, 114
Wuyts, S., Förster Schreiber, N. M., Lutz, D., et al. 2011a, ApJ, 738, 106
Wuyts, S., Förster Schreiber, N. M., Nelson, E. J., et al. 2013, ApJ, 779, 135
Wuyts, S., Förster Schreiber, N. M., van der Wel, A., et al. 2011b, ApJ, 742, 96
Wuyts, S., Labbé, I., Franx, M., et al. 2007, ApJ, 655, 51
Wuyts, S., Labbé, I., Schreiber, N. M. F., et al. 2008, ApJ, 682, 985
Yang, X., Mo, H. J., van den Bosch, F. C., Zhang, Y., & Han, J. 2012, ApJ, 752, 41
Yoshikawa, T., Akiyama, M., Kajisawa, M., et al. 2010, ApJ, 718, 112
Yuan, T.-T., Kewley, L. J., Swinbank, A. M., Richard, J., & Livermore, R. C. 2011, ApJL, 732, L14
Zahid, H. J., Geller, M. J., Kewley, L. J., et al. 2013, ApJL, 771, L19
Zheng, X. Z., Bell, E. F., Papovich, C., et al. 2007, ApJL, 661, L41